Extreme weather in the Southern Hemisphere in early 2022

Andries Jan de Vries,[a] Wolfgang Wicker,[a] Georgios Fragkoulidis,[b] Irina Rudeva,[c] Pauline Rivoire,[a,d] Emmanuele Russo,[e] Jake W. Casselman,[e] Priyanka Yadav,[e,f,g] Romain Pilon,[a] Hilla Afargan-Gerstman,[a,e] Shingirai Nangombe,[h,i] Neil C. G. Hart,[j] Daniela I. V. Domeisen[a,e]

[a] *Institute of Earth Surface Dynamics, University of Lausanne, Lausanne, Switzerland*

[b] *Institute of Environmental Research and Sustainable Development, National Observatory of Athens, Athens, Greece*

[c] *Australian Bureau of Meteorology, Melbourne, Australia*

[d] *School of Architecture, Civil and Environmental Engineering (ENAC), Ecole Polytechnique Fédérale de Lausanne (EPFL), Lausanne, Switzerland*

[e] *Institute for Atmospheric and Climate Science, ETH Zürich, Zürich, Switzerland*

[f] *Earth System Science Interdisciplinary Center (ESSIC), University of Maryland, College Park, MD, USA*

[g] *Global Modeling and Assimilation Office, NASA Goddard Space Flight Center, Greenbelt, MD, USA*

[h] *National Center for Climate Research, Danish Meteorological Institute, Copenhagen, Denmark*

[i] *Holistic Climate Change impact area, Council for Scientific and Industrial Research, Pretoria, South Africa*

[j] *School of Geography and the Environment, University of Oxford, Oxford, United Kingdom of Great Britain – England, Scotland, Wales*

Corresponding author: Andries Jan de Vries, andries-jan.devries@unil.ch

Early Online Release: This preliminary version has been accepted for publication in *Bulletin of the American Meteorological Society*, may be fully cited, and has been assigned DOI 10.1175/BAMS-D-23-0141.1. The final typeset copyedited article will replace the EOR at the above DOI when it is published.

CAPSULE

A multiscale analysis of the atmospheric processes leading to deadly floods in eastern Australia and South Africa and an unprecedented heatwave in Antarctica in early 2022.

ABSTRACT

In early 2022, several exceptionally extreme weather events struck the Southern Hemisphere. Deadly floods affected eastern Australia and South Africa, and an unprecedented heatwave in East Antarctica broke global temperature anomaly records. This study presents a multi-scale analysis of the atmospheric processes leading to these extreme events ranging from local to planetary scales. While the subtropical flood events were associated with slow-moving circulation patterns with moderate departures from climatology, the Antarctic heatwave was unprecedented with surface temperatures and atmospheric moisture content breaking records in observation-based data since 1979. Despite the variety in weather type and region, all three extreme events share the commonality that they result from extratropical Rossby wave breaking modulated by tropical variability on intraseasonal to interannual timescales. Equatorward wave breaking steered moisture transport from nearby oceans towards the subtropical flood regions favored by anticyclonic circulation anomalies in the midlatitudes and a poleward displaced midlatitude jet. Enhanced tropical convection over the Indian Ocean promoted poleward-eastward Rossby wave propagation eventuating in poleward wave breaking that forced an intrusion of exceptionally warm and moist air masses into the Antarctic continent. At seasonal timescales, large parts of the study regions experienced record-breaking surface weather associated with the influence of La Nina setting up favorable circulation patterns for heavy precipitation over the eastern Australian and South African coasts and heatwave occurrence over East Antarctica's interior. This study contributes to an improved process-understanding of extreme weather events in the Southern Hemisphere with implications for weather and climate prediction of such events.

SIGNIFICANCE STATEMENT

Within a two-month period in early 2022, eastern Australia and South Africa incurred unprecedented flood impacts and Antarctica experienced a heatwave breaking global temperature anomaly records. Our collaborative effort investigates the local and remote atmospheric processes leading to these extreme events. We find that all three extreme weather events have a common origin in wave breaking in the midlatitude circulation influenced by tropical weather and climate variability. Future research evaluating the simulation of these

Accepted for publication in *Bulletin of the American Meteorological Society.* DOI 10.1175/BAMS-D-23-0141.1.

wave breakings in weather and climate models is an important step towards improving predictions and projections of extreme weather with high impacts on society and the polar cryosphere.

KEY WORDS

flooding, heatwaves, extreme weather events, Rossby waves, El Niño Southern Oscillation, Madden-Julian Oscillation, Southern Hemisphere, Antarctica.

Introduction

In early 2022, the Southern Hemisphere experienced several exceptionally extreme weather events. Deadly floods occurred on the South American (Alcântara et al., 2023; Marengo et al., 2023), African, and Australian continents, multiple tropical cyclones struck southeastern Africa and Australia (Otto et al., 2022), and a heatwave broke temperature records in the coldest region on Earth, Antarctica. This article focuses on three of these extreme events that were unprecedented in terms of their impacts on society or their levels of extremeness in surface weather. At the end of February 2022, record-breaking extreme precipitation and flooding affected eastern Australia (Fryirs et al., 2023; Gillett et al., 2023a; Reid et al., 2025) causing 22 fatalities and 6.6 billion USD in damage, including 3.9 billion USD in insured damage, making this event the costliest natural disaster in the country's history in terms of insurance losses according to the Emergency Event Database (EM-DAT; Table 1). In mid-March, Antarctica experienced the largest ever recorded temperature anomaly globally (Blanchard-Wrigglesworth et al., 2023), impacting the continent's cryosphere, including coastal ice melt, the final collapse of the Conger ice shelf, and extreme precipitation over the interior of the continent (Wille et al., 2024a,b). In April, floods ravaged South Africa's southeastern coast leaving 544 deaths and 3.5 billion USD in damage, making this the deadliest and costliest natural disaster in South Africa's history (Table 1; Grab and Nash, 2023).

The notable occurrence of these three extreme weather events within a period of less than 2 months, the unprecedented flood impacts, and the record-breaking temperature extreme motivate this study to elucidate the atmospheric drivers of these extreme events and to examine whether they had a common underlying cause making these extreme events more likely to occur. To this end, we quantify the extremeness of the surface weather and atmospheric

Accepted for publication in *Bulletin of the American Meteorological Society.* DOI 10.1175/BAMS-D-23-0141.1.

conditions, identify the driving synoptic-scale processes, and examine the influence of prominent atmosphere and climate variability modes - the Madden-Julian Oscillation (MJO) and El-Nino Southern Oscillation (ENSO) - on the occurrence of these extreme events in a climatological context. This study shows that the three extreme events, despite their different weather types and locations, have a common atmospheric driver: the breaking of extratropical Rossby waves modulated by tropical weather and climate variability. The findings presented in this study are supported by a range of diagnostics, the methods of which are detailed in Appendix A.

Table 1. Natural disaster impacts in Australia and South Africa[1,2]

No.	Date	Disaster type	Location	Deaths	Affected people	Insured damage USD (million)	Damage USD (million)
Top 10 natural disasters in Australia ranked according to insured damages							
1	**22 Feb - 3 Mar 2022**	**Flood**	**Queensland, New South Wales**	**22**	**54,000**	**3,900**	**6,600**
2	25 Dec 2010 – 4 Feb 2011	Flood	New South Wales, Queensland, Victoria	35	175,000	2,500	7,300
3	27 Mar – 6 Apr 2017	Storm	Queensland	12	45,000	1,400	2,700
4	2-5 Feb 2011	Storm	Queensland	1	7,300	1,300	2,500
5	14 Apr 1999	Storm	Sydney	1	6024	1,100	1,500
6	19-21 Jan 2020	Storm	New South Wales, Victoria States			1,000	1,500
7	23-30 Jan 2013	Storm	Queensland, New South Wales	6	7,500	1,000	2,000
8	22 Mar 2010	Storm	Western Australia			990	1,390
9	6-10 Mar 2010	Storm	Victoria, New South Wales, Tasmania			950	1,330
10	13-26 Feb 2008	flood	Queensland	2	1,000	890	1,100
Top 10 natural disasters in South Africa ranked according to number of deaths							
1	**8-18 Apr 2022**	**Flood**	**Durban, KwaZulu-Natal province**	**544**	**142,290**	**1,800**	**3,500**
2	25-29 Sep 1987	Flood	Natal, KwaZulu	506	65,000	248	765
3	25 Dec 1995 – 2 Jan 1996	Flood	KwaZulu-Natal province	207	4,500		10
4	19 Aug 2000 – 16 Apr 2001	Epidemic	KwaZulu-Natal province	181	86,107		
5	Jan 1981	Flood	Cape province	104			1
6	26 Jan – 27 Mar 2000	Flood	Mpumalanga, KwaZulu-Natal, Gauteng provinces	83		50	160
7	21-25 Apr 2019	Flood	KwaZulu-Natal, Eastern Cape, Free state provinces	73	1,000		50
8	1-1-2002	Epidemic	Eastern Cape, KwaZulu-Natal, Northern provinces	72	12,927		
9	15 Nov 2008 – 31 May 2009	Epidemic	Limpopo, Mpumalanga, Gauteng provinces	65	12,752		
10	28 Jan – 4 Feb 1984	Storm	Natal, Kwazulu, Transvaal	64	500,000		92
Top 10 natural disasters in South Africa ranked according to total damage							
1	**8-18 Apr 2022**	**Flood**	**Durban, KwaZulu-Natal province**	**544**	**142,290**	**1,800**	**3,500**
2	May 2017-Jun 2018	Drought	Western Cape, Eastern Cape, Northern Cape				1,200
3	1991-Mar 1992	Drought	Northern and eastern Transvaal, central and northern Natal, eastern and northern Cape				1,000
4	25-29 Sep 1987	Flood	Natal, KwaZulu	506	65,000	248	765
5	30 Aug - 3 Sep 2008	Wildfire	KwaZulu-Natal, Free state	34	25		430
6	7 - 13 Jun 2017	Wildfire	Knysna (Eden)	9	5,500	200	420
7	20 Mar 1990	Storm	Welkom, Natal	2		118	393

Accepted for publication in *Bulletin of the American Meteorological Society.* DOI 10.1175/BAMS-D-23-0141.1.

8	9-10 Oct 2017	Storm	Durban, Johannesburg, Ekurhuleni, West Rand District Municipality, Nquthu	11	518	140	320
9	7-8 Jun 2017	Storm	Cape Town, Eden, Cape Winelands	9	6,918	145	283
10	Jan 2015 - May 2017	Drought	KawZulu-Natal, Free state, Limpopo, Mpumalanga, North-West, Western Cape provinces		2,700,000		250

[1]) data records are retrieved from the Emergency Event Database (EM-DAT), accessed on 24 May 2024
[2]) text in bold refers to the event discussed in this study

Surface weather and its extremeness

The extremeness of surface weather can be measured by its peak intensity, duration, spatial extent, and integrated intensity across time and space. Here we present an overview of the three extreme events, and we examine the extremeness of the corresponding surface weather at daily and multi-day event timescales (Fig. 1). Throughout the manuscript, we first discuss the east Australia and South Africa flooding and then the Antarctic heatwave.

Eastern Australia experienced widespread heavy precipitation from 22 to 28 February (Fig. 1a). At multiple weather stations, the extreme precipitation broke previous records at daily and weekly timescales since measurements began in 1900 (Bureau of Meteorology, 2022). According to reanalysis-based estimates, the intensity of daily precipitation peaked on 24 February with a largest local return period (see Appendix A) of nearly 1-in-100 years, corresponding to 150 mm, and a total precipitation volume of 12 km^3 over the region of interest (Fig. 1b). This was the 2nd most extreme precipitation day considering the local and regional precipitation intensity combined during the period of 1979-2022. At multi-day event timescales, the February 2022 event ranks 6th in total precipitation volume, with 48 km^3 of water falling as precipitation, among precipitation events defined by consecutive days with an area-average precipitation greater than 5 mm day^{-1} (Fig. 1e). Antecedent moist soil conditions associated with a previous La Niña year contributed to a rapid saturation of catchments and widespread riverine flooding and flash floods (Bureau of Meteorology, 2022; Fryirs et al., 2023; Gillett et al., 2023a; Huang et al. 2024; Reid et al., 2025). Other rainfall episodes followed in early and late March extending over southeastern Australia, claiming another 4 lives (EM-DAT). The primary focus of this study is on the first extreme precipitation episode at the end of February that brought the largest precipitation amounts and inflicted the most severe societal impacts.

Accepted for publication in *Bulletin of the American Meteorological Society.* DOI 10.1175/BAMS-D-23-0141.1.

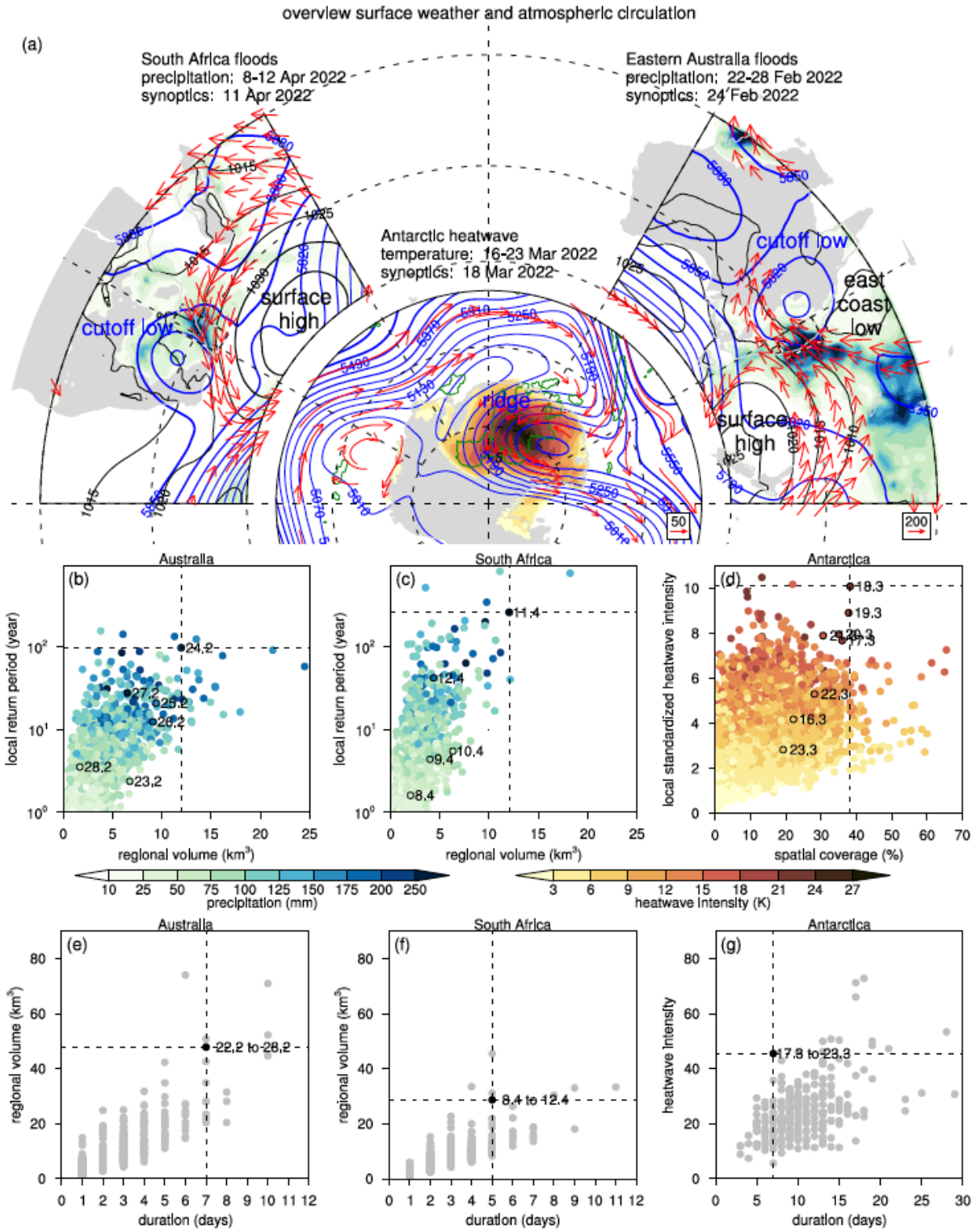

Figure 1. (a) Synoptic overview of the three extreme weather events and the extremeness of surface weather at (b)-(d) daily and (e)-(g) multi-day event timescales. In (a) ERA5 precipitation sums over the east Australian and South African domains and the largest daily 2m temperature anomaly above the heatwave threshold over the Antarctic domain, land only, during the periods indicated in text. Furthermore, in (a) daily means of 500-hPa geopotential height in blue contours at 30 gpm (eastern Australia and South Africa) and 60 gpm (Antarctica) intervals, sea level pressure in black contours at 5 hPa intervals (eastern Australia and South Africa only), and IVT in red vectors only plotted for a magnitude larger than 200 kg m^{-1} s^{-1} (eastern Australia and South Africa) and 50 kg m^{-1} s^{-1} (Antarctica) on the days indicated in text. Green contours in the Antarctic domain encircle daily precipitation exceeding the 99.9th percentile during 16-23 March 2022

Accepted for publication in *Bulletin of the American Meteorological Society.* DOI 10.1175/BAMS-D-23-0141.1.

with reference to the period of 1979-2022. In (b), for each day in the year-round period of 1979-2022, the largest return periods of ERA5 daily precipitation at the grid scale (y-axis), the corresponding precipitation amount (colors), and the total precipitation volume (x-axis) across a subregion over eastern Australia (150-154°E, 25-31°S), land only. In (c), as (b), but for a subregion over South Africa (29-33°E, 26-34°S), land only. In (d), for each day in the period of 1959-2022, the largest local standardized heatwave intensity across Antarctica (y-axis), the corresponding temperature anomaly above the heatwave threshold (colors), and the fraction of the Antarctic surface area experiencing a heatwave on that day. In (e) the duration and total volume of precipitation events over the east Australia subregion. In (f), as (e), but for the South Africa subregion. In (g) the intensity and duration of the most extreme heatwaves across Antarctica based on the largest local heatwave intensity per season. The days and event periods of the studied extreme weather events are indicated in text in (b)-(d) and (e)-(g), respectively. The subregions over South Africa and eastern Australia are indicated in (a) in black-white dashed lines.

Turning to the South Africa flooding, heavy precipitation occurred during the period of 8 to 12 April, with the largest amounts falling over the southeastern coast in the KwaZulu Natal province on 11 April (Fig. 1a,c). Several stations measured over 300 mm day^{-1} on 11 April, while the Margate station recorded more than 500 mm during the three-day period of 10-12 April (Thoithi et al., 2023). Reanalysis-based precipitation intensity peaked on 11 April, locally exceeding a 1-in-250-year return period along with a 12 km^3 precipitation volume over the region (Fig. 1c). Similar to the east Australia flooding, only one other single day during the period of 1979 to 2022 received more intense precipitation at the local and regional scale combined (dot in the upper-right quadrant in Fig. 1b,c). During the event, southeastern Africa received more than 28 km^3 of water as precipitation, yielding a ranking as the 7th most severe precipitation event in terms of the regional precipitation volume (Fig. 1f). Pinto et al. (2022) estimated, based on ERA5 reanalysis, that the return period of the extreme precipitation at the regional scale during the two-day period of 11-12 April is 20 years under present-day climate conditions.

The Antarctic heatwave of March 2022 shattered multiple temperature records. (Sub)daily temperature records were broken for the month of March at the Vostok and Concordia stations as well as over nearly 25% of the continent's surface (Wille et al., 2024a). The March 2022 heatwave was the largest ever recorded temperature anomaly globally with daily mean temperatures of 39°C above climatology (Blanchard-Wrigglesworth et al., 2023). Given the limited number of station observations over Antarctica, we use ERA5 reanalysis data to portray the heatwave characteristics and its extremeness from the local to continental scale. The March 2022 heatwave lasted from 16 to 23 March, extended over nearly 40% of Antarctica, and reached near-surface air temperature anomalies of 27°C above the heatwave threshold used in

Accepted for publication in *Bulletin of the American Meteorological Society.* DOI 10.1175/BAMS-D-23-0141.1.

this study (Fig. 1a,d), detailed in Appendix A. Locally, the heatwave intensity peaked on 18 March with temperatures, accounting for seasonal variability, exceeding 10 standardized anomalies above usual heatwave conditions in the region (Fig. 1d). This extremely large anomaly occurred farther poleward from the Concordia station (Fig. 2a) where Blanchard-Wrigglesworth et al. (2023) and Wille et al. (2024a) reported a temperature anomaly of 6 standard deviations above the mean. While Fig. 1d shows that extremely high standardized heatwave intensities also occurred on other occasions, no other day exceeded the combined intensity and spatial extent of the heat extreme on 18 March 2022 (Fig. 1d). At the event-scale, the March 2022 heatwave had a relatively short duration of 7 days, but the largest intensity - measured by the time integrated standardized temperature anomalies - among all heatwaves with a duration of less than 10 days (Fig. 1g).

Synoptic-scale processes

Atmospheric processes at synoptic scales – on the order of 1,000 km and from one to several days – are of major interest to meteorologists to understand and predict daily weather and extreme events. Figure 1a depicts the prevailing synoptic circulation patterns that characterized the three extreme weather events. Consistent with findings of previous studies, the east Australia and South Africa floods were linked to upper-tropospheric cutoff lows (Mashao et al., 2023; Barnes et al., 2023; Thoithi et al., 2023), while the Antarctic heatwave was associated with an atmospheric ridge (Wang et al., 2023; Blanchard-Wrigglesworth et al., 2023; Wille et al., 2024a).

During the east Australia and South Africa floods, the upper-tropospheric cyclonic circulations were associated with the formation of surface cyclones. Near Australia's east coast, multiple surface cyclones developed and remained quasi-stationary over the Coral Sea (Gillett et al., 2023a; Barnes et al., 2023), where the formation of such "east coast lows" is common (Dowdy et al., 2019). For the South Africa case, a mesoscale low - which became subtropical cyclone Issa - formed on 11 April over the warm Agulhas current and tracked southward along the South African coast until deflecting southeastward on 13 April (Thoithi et al., 2023). Furthermore, both flood events were accompanied by near-surface anticyclonic circulation patterns to the southeast of the Australian and South African coasts (Fig. 1a). This atmospheric configuration, consisting of a deep cyclonic circulation over the subtropics and a surface

Accepted for publication in *Bulletin of the American Meteorological Society.* DOI 10.1175/BAMS-D-23-0141.1.

anticyclonic circulation over the midlatitudes, sets up a strong easterly moist air flow towards the coastal regions (Fig. 1a), supporting the formation of heavy precipitation over these regions, as previously noted for both flood events (Barnes et al., 2023; Thoithi et al., 2023) as well as rainfall over South Africa and southeastern Australia (Ndarana et al., 2020; Holgate et al. 2023). Orographic lifting of the moist air masses in combination with dynamically forced ascent - that can be expected on the downstream flanks of the cutoff lows - constitute mechanisms that initiate and sustain deep moist convection (Barnes et al., 2023; Thoithi et al., 2023). The pivotal role of cutoff lows is not limited to these two flood events, but has been widely documented for extreme precipitation and flooding in the Southern Hemisphere, specifically over southeastern Australia (Risbey et al., 2009; Grossfeld et al., 2021; Warren et al., 2021;), South Africa (Singleton and Reason, 2007; Favre et al., 2013; Hart et al., 2013; Barnes et al., 2021), and Chile (Rondanelli et al., 2018; Reyers et al., 2021; Muñoz and Schultz, 2021).

In contrast to the subtropical flood events, the Antarctic heatwave was associated with an atmospheric ridge reaching far into the Antarctic continent (Fig. 1a; Wang et al., 2023; Blanchard-Wrigglesworth et al., 2023; Wille et al., 2024a). On the upstream flank of the ridge, strong poleward winds transported very warm and moist air masses into the continent that not only contributed to the unprecedented heatwave but also to extreme precipitation along Antarctica's coastline and the interior of the continent (Figure 1a, Wille et al., 2024b). Elongated structures of intense horizontal moisture transport, also known as "atmospheric rivers", have been linked to this specific heatwave (Wille et al., 2024a) as well as to other temperature and precipitation extremes over Antarctica (Hepworth et al., 2022; Turner et al., 2022; Wille et al. 2022; Simon et al., 2024). Atmospheric processes contributing to atmospheric hot extremes include horizontal warm air advection, adiabatic warming of subsiding air, and diabatic heating resulting from radiative processes (Röthlisberger and Papritz, 2023). While the horizontal advection of warm air (Blanchard-Wrigglesworth et al., 2023) and trapping of longwave radiation by low-level clouds (Wille et al., 2024a,b) played important roles for the Antarctic heatwave of March 2022, their relative contributions to this heatwave remain to be quantified but are beyond the scope of this present study.

Extremeness of the atmospheric conditions

Accepted for publication in *Bulletin of the American Meteorological Society.* DOI 10.1175/BAMS-D-23-0141.1.

To further examine the atmospheric characteristics under which the three extreme weather events developed, we compute standardized anomalies of atmospheric dynamic and thermodynamic conditions with respect to local climatology (see Appendix A). During the subtropical flood events, 500-hPa geopotential height anomalies associated with the cutoff lows reached locally between 1 and 2.5 standard deviations below normal conditions (Fig. 2a,b,c). Similarly, total atmospheric water content attained locally 1.5 to 4 standard deviations above normal conditions (Fig. 2a,b,c). Vertically integrated horizontal water vapor transport (IVT) reached up to 4 and over 6 standard deviations above normal from primarily easterly directions during the east Australia and South Africa events, respectively (Fig. 2e,f).

In contrast to the subtropical flood events, the atmospheric dynamic and thermodynamic conditions during the Antarctic heatwave reached extremely high to record-breaking departures from climatology. Locally, 500-hPa geopotential height anomalies associated with the atmospheric ridge exceeded 5 standard deviations above normal on 17 March, while the total atmospheric water content reached nearly 16 standard deviations above normal on 18 March, the largest standardized anomaly ever recorded across all of Antarctica during the period from 1979 to 2022 (Fig. 2a,d). Moisture transport anomalies exceeded 15 standard deviations above normal in both zonal and meridional directions on 17 and 18 March, ranking as the 3rd and 2nd largest extreme, respectively, based on the zonal and meridional components combined (Fig. 2g).

Our findings suggest that the subtropical extreme precipitation events formed under the influence of circulation patterns with relatively moderate anomalies that maintained steady moisture transport (Barnes et al. 2023). On the other hand, the Antarctic heatwave of March 2022 resulted from extremely strong atmospheric forcing, consistent with the occurrence of record-breaking heatwaves elsewhere, for example, over western North America (Bartusek et al., 2022).

Accepted for publication in *Bulletin of the American Meteorological Society.* DOI 10.1175/BAMS-D-23-0141.1.

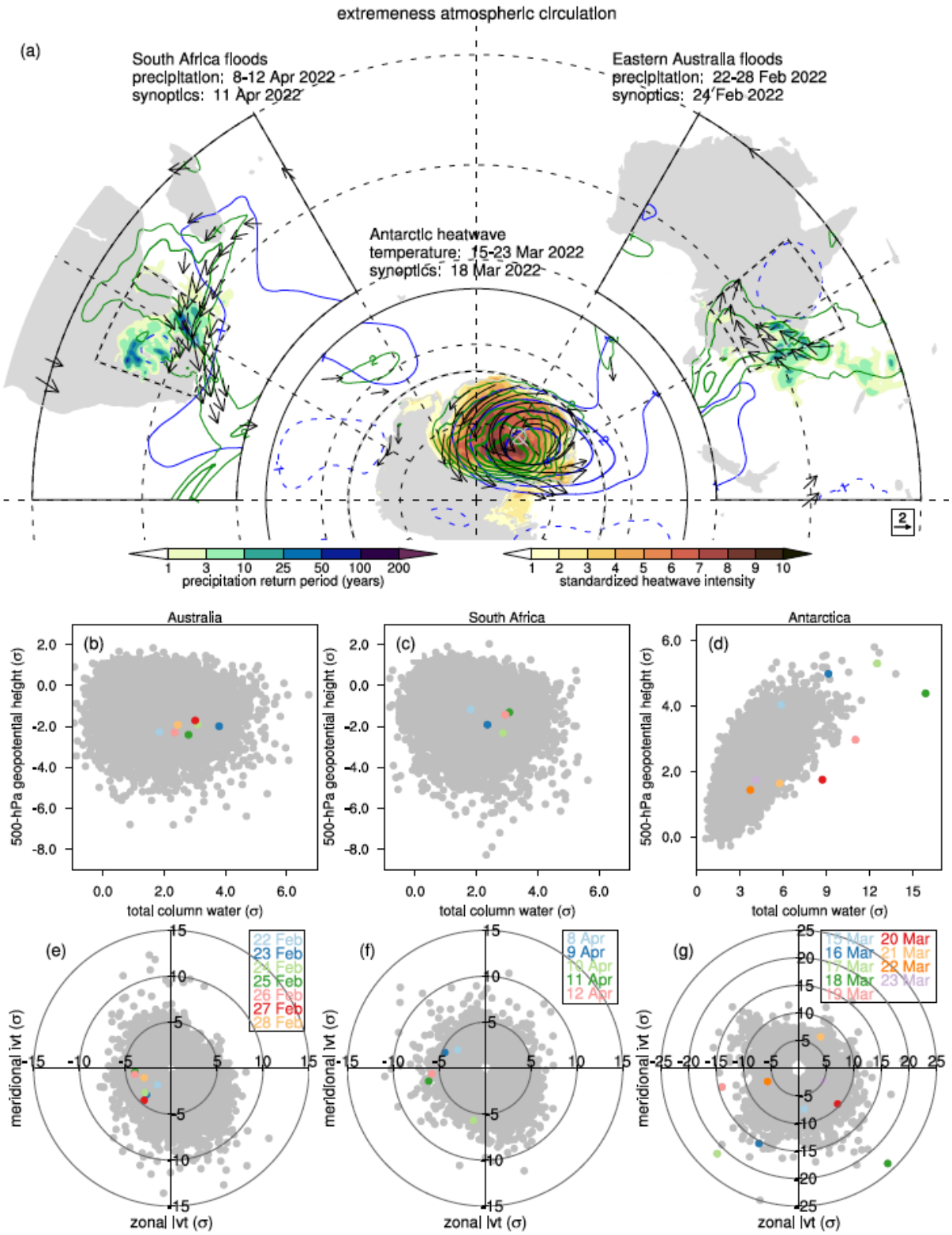

Figure 2. (a) overview of the extremeness of the surface weather and atmospheric conditions during the three extreme weather events and (b)-(g) the extremeness of the daily atmospheric conditions in climatological context. In (a) the largest return periods of daily ERA5 precipitation over east Australian and South African domains and the largest daily standardized heatwave intensity over the Antarctic domain, land only, during the periods indicated in text. Furthermore, in (a) standardized anomalies of daily mean 500-hPa geopotential height in blue contours with positive values in solid and negative values in dashed at

Accepted for publication in *Bulletin of the American Meteorological Society.* DOI 10.1175/BAMS-D-23-0141.1.

1 standard deviation intervals (all three domains), total column water in green contours for positive values only at 1 standard deviation (eastern Australia and South Africa) and 2 standard deviation (Antarctica) intervals, and zonal and meridional IVT components in black vectors, only plotted when exceeding a magnitude of 2 standard deviation (all three domains). The light gray marker depicts the location of the Concordia station (123.3°E, 75.1°S). In (b), for each day in the period of 1979-2022, the largest positive local standardized anomaly in total column water and the largest negative local standardized anomaly in 500-hPa geopotential height over eastern Australia (140-155°E, 20-35°S). In (c), as (b), but for South Africa (20-35°E, 20-35°S). In (d), as (b), but for the largest positive local standardized anomaly in 500-hPa geopotential height over Antarctica (0-360°E, 65-90°S). The selected regions are indicated in black-white dashed boxes in (a). In (e)-(g), as (b)-(d), but for zonal and meridional IVT whereby the local daily maxima values over the regions are defined based on grid points with the largest values in standardized anomalies of zonal and meridional IVT combined. The days during the studied extreme weather events are indicated by colors in (b)-(g) as shown in the legend.

A Rossby wave breaking perspective

The presence of upper-tropospheric cutoff lows and ridges during the extreme weather events suggests an important role of atmospheric Rossby waves in the formation of these extreme events. Rossby waves arise in the extratropical circulation due to the Earth's rotation and sphericity (Wirth et al., 2018). When these waves amplify, they can overturn and break, going along with the formation of troughs, ridges, and cutoffs (Ndarana and Waugh, 2010; Pérez-Fernández et al., 2024). The upper-level forcing can extend to - and interact with - the lower tropospheric circulation and contribute to the formation of surface cyclones and anticyclones (Ndarana et al., 2018, 2023; Portmann et al., 2021; Pinheiro et al., 2024; Tamarin-Brodsky and Harnik, 2024) as well as extreme weather events including heatwaves (Parker et al., 2014; Fragkoulidis et al., 2018; Ali et al., 2022; Wicker et al., 2024; Henderson et al., 2024), cold, hot, and wet spells (Röthlisberger et al., 2019; Ali et al., 2021) and heavy precipitation (Grazzini et al., 2021; Jin et al., 2024). To diagnose the breaking of Rossby waves, we adopt a potential vorticity (PV) framework and identify elongated and isolated PV contours, so-called PV streamers and cutoffs, at a range of isentropic levels with 5 K intervals (see Appendix A). Figure 3a shows the objectively identified PV structures and their vertical extent during the three episodes of interest, demonstrating the occurrence of Rossby wave breaking (RWB) during all three extreme weather events. Blue (green) shading denotes PV structures with cyclonic (anticyclonic) PV anomalies signifying equatorward (poleward) RWB.

Both the east Australia and South Africa flooding were accompanied by RWB on the equatorward side of the midlatitude jet (Fig. 3a). For the east Australia flooding (22-28 February), two consecutive RWB events occurred, the first one lasting from 21 to 24 February and the second from 26 February to 1 March 2022 (Fig. 3b and Fig. B1a). For the South Africa

Accepted for publication in *Bulletin of the American Meteorological Society.* DOI 10.1175/BAMS-D-23-0141.1.

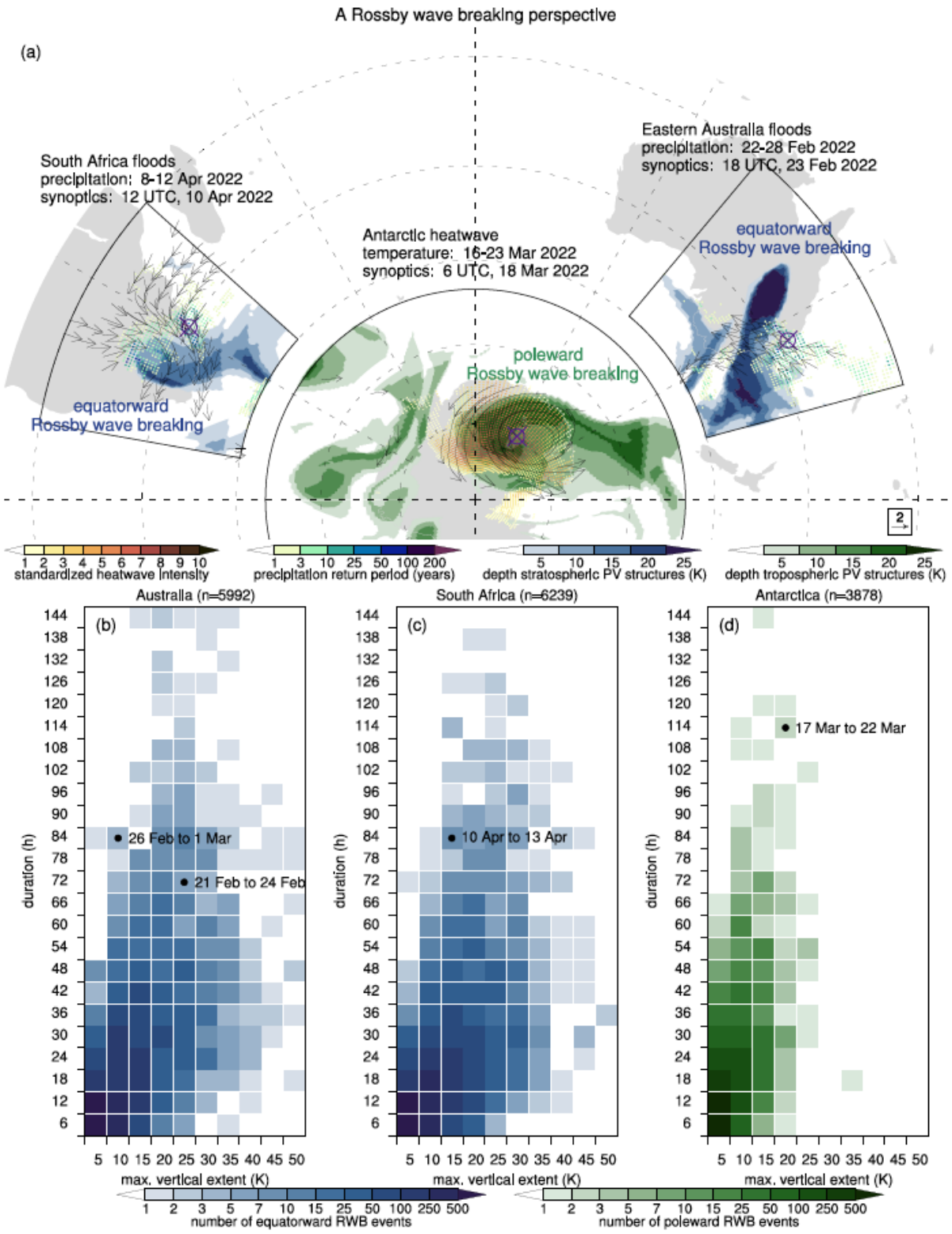

Figure 3. (a) a Rossby wave breaking perspective on the three extreme weather events and (b)-(d) the extremeness of the wave breaking characteristics in climatological context. In (a), as in Fig. 2a, the largest return periods of daily ERA5 precipitation (green-blue dots) over eastern Australia and South Africa and the largest daily standardized heatwave intensity (yellow-red dots) over the Antarctic continent during the periods indicated in text. Furthermore, in (a) the vertical extent of equatorward RWB (blue shading) and poleward RWB (green shading), which is based on the number of isentropic surfaces on which PV streamers and cutoffs are detected, and the standardized anomalies of daily mean zonal and meridional IVT in black vectors if exceeding a magnitude of 2 standard deviations, for the days indicated in text. In (b), the

Accepted for publication in *Bulletin of the American Meteorological Society.* DOI 10.1175/BAMS-D-23-0141.1.

frequency distribution of RWB events (1979-2022) as a function of the duration and maximum vertical extent of stratospheric PV structures at a location (147°E, 30°S) approximately 5 degrees west of the flood affected city Brisbane, eastern Australia. In (c), as (b), but for a location (25°E, 30°S), approximately 5 degrees west of Durban, South Africa. In (d), as (b), but for tropospheric PV structures at the Concordia station (123.3°E, 75.1°S). The duration of RWB events occurring during the studied extreme weather events are indicated in text.

case (8-12 April), RWB commenced on 9 April over southwestern South Africa and dominated over southeastern South Africa from 10-13 April (Fig. 3c and Fig. B1b). In both flood regions, the arrival of RWB goes along with cyclonic activity and a strengthening of the northeasterly moisture transport towards the regions of extreme precipitation (Fig. 3a and Fig. B1a,b). In a PV framework, this can be understood by the fact that upper-tropospheric cyclonic PV anomalies can induce a cyclonic circulation in the lower troposphere, intensifying the near-surface easterly-northeasterly winds at the southeastern flanks of the upper-tropospheric cyclonic PV anomalies. RWB can further support the formation of heavy precipitation by inducing quasi-geostrophic ascent at its downstream flank, potentially destabilizing the troposphere by the lifting of moist air layers (Schlemmer et al 2010; De Vries, 2021). The importance of RWB for the occurrence of the subtropical flood events is consistent with previous studies linking this atmospheric process to extreme precipitation over (south)eastern Australia and South Africa (Barnes et al., 2021, 2023; De Vries, 2021, Ivancu et al., 2022; De Vries et al., 2024; Reid et al., 2025).

The Antarctic heatwave formed under the influence of RWB on the poleward side of the midlatitude jet (Fig. 3a). The poleward breaking wave is associated with an anticyclonic PV anomaly extending into Antarctica, inducing a strong anticyclonic circulation in the lower troposphere. Accordingly, the poleward breaking wave contributed to near-surface temperature extremes through transporting very warm air masses from the extratropics into high latitudes at its upstream (western) flank (Blanchard-Wrigglesworth et al., 2023) and through enhancing atmospheric water content to extremely high levels that supported the formation of low-level clouds trapping longwave radiation underneath these clouds (Wille et al., 2024a,b). A local perspective from the Concordia station shows that the intensification of the poleward atmospheric moisture transport coincides with the poleward wave breaking which remained over this location from 17 to 22 March (Fig. 3d and Fig. B1c). While previous studies have documented the role of RWB in modulating moist air intrusions into the Arctic (Woods et al.,

Accepted for publication in *Bulletin of the American Meteorological Society.* DOI 10.1175/BAMS-D-23-0141.1.

2013; Liu and Barnes, 2015), we show here for the first time that poleward RWB plays a central role in the formation of an unprecedented heatwave over Antarctica.

To further examine the role of RWB characteristics in the occurrence of the three extreme weather events, we quantify the duration and maximum vertical extent of the PV structures during these events as a measure of the wave breaking stationarity and intensity, respectively. The duration is defined by the consecutive 6-h timesteps at which a PV structure covers the location in question and the maximum vertical extent by the largest number of isentropic levels at which PV structures occur during each RWB event. For both subtropical flood events, the breaking waves had notable durations of approximately 72 and 84 hours, ranking within the top 200 and 100, respectively, of a total of approximately 6000 RWB events over eastern Australia and South Africa (Fig. 3b,c). The maximum vertical extent of the PV structures was relatively modest with 25 K and 10 K for the RWB events over eastern Australia during 21-24 February and 26 February – 1 March, respectively, and 15 K for the RWB event over South Africa during 10-13 April. For the Antarctic heatwave, the poleward RWB was exceptionally extreme in both duration and intensity, lasting approximately 114 hours and having a vertical extent of 20 K (Fig. 3d). At this location, only three other RWB events had a longer duration, 20 RWB events had a larger vertical extent, and only one RWB event had a longer duration combined with an equivalent vertical extent. The very extreme nature of the poleward RWB event during the March 2022 Antarctic heatwave is consistent with the 500-hPa geopotential height standardized anomaly ranking within the top-10 on 17 March (Fig. 2d).

The influence of the MJO

At intraseasonal timescales, the MJO is a leading mode of atmospheric variability influencing weather and climate globally (Zhang, 2012). This oscillation manifests as organized deep convection over the tropics moving slowly eastward across the Indian and Pacific Oceans with a periodicity of approximately 30-90 days (Madden and Julian, 1972). During February-March 2022, the MJO was active over the Indian Ocean as shown by the predominance of MJO phases 1-4 with an amplitude larger than 1 (Fig. 4).

Accepted for publication in *Bulletin of the American Meteorological Society.* DOI 10.1175/BAMS-D-23-0141.1.

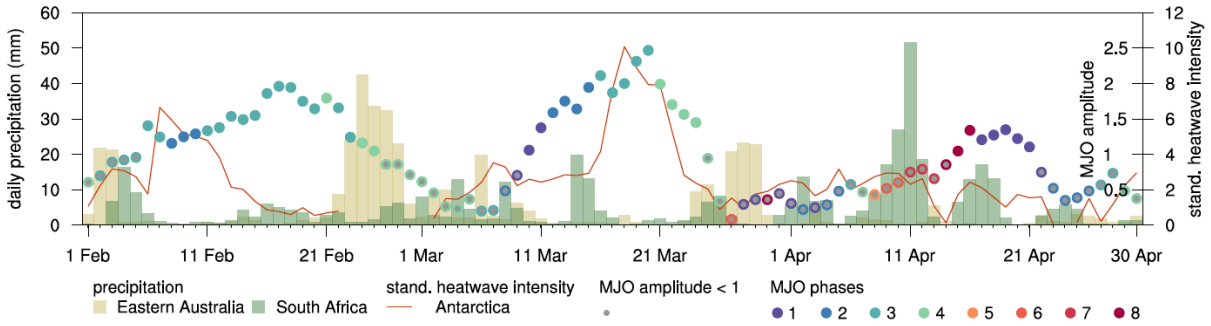

Figure 4. Timeseries of daily area-average precipitation over eastern Australia (150-154°E, 25-31°S) and South Africa (29-33°E, 26-34°S), land only, maximum local daily standardized heatwave intensity across Antarctica, and the MJO amplitude and phase, see the legend.

Previous studies demonstrated a positive association between east Australia precipitation and the MJO phases 3 to 5 during austral summer and autumn (Wheeler et al., 2009; Dao et al. 2023; Cowan et al., 2023). Indeed, a strong MJO evolved from phase 3 to phase 4 during a 10-day period prior to both extreme precipitation episodes over eastern Australia at the end of February and at the end of March 2022 (Fig. 4). To further examine the influence of enhanced tropical convection over the eastern Indian Ocean and Maritime Continent on east Australia precipitation, we construct time-lagged composites of anomalies in precipitation and the atmospheric circulation for MJO phase 4 events during the period of 1979-2021 (see Appendix A). We observe a weak and marginally significant precipitation increase along the east Australia coast in the two pentads following MJO phase 4 events (Fig. B2b,c). 500-hPa geopotential height composites exhibit positive and negative anomalies to the south of Australia and over eastern Australia, respectively (Fig. B2d,e,f), resembling the circulation anomalies as observed at the end of February 2022. Signals in equatorward RWB frequencies are spatially less coherent and depict a local increase over north Australia during the pentad 0 to +4 days (Fig. B2h).

Switching to South Africa, previous work indicated that MJO phase 6-8 is linked to a moderate increase in the likelihood of precipitation extremes over this region (Hart et al., 2013; Ullah et al., 2023). The MJO was indeed in phase 6 and 7 during 9 to 13 April, albeit in weak state with an amplitude < 1 (Fig. 4). Composites for the MJO phase 6 indicate a weak non-significant precipitation increase over South Africa. Significant cyclonic circulation anomalies over South Africa and anticyclonic circulation anomalies over the Southern Atlantic (Fig. B3) are consistent with the circulation patterns as observed during the April 2022 flood, and may

Accepted for publication in *Bulletin of the American Meteorological Society.* DOI 10.1175/BAMS-D-23-0141.1.

thus lend some support for a possible role of the MJO in the South Africa extreme precipitation event.

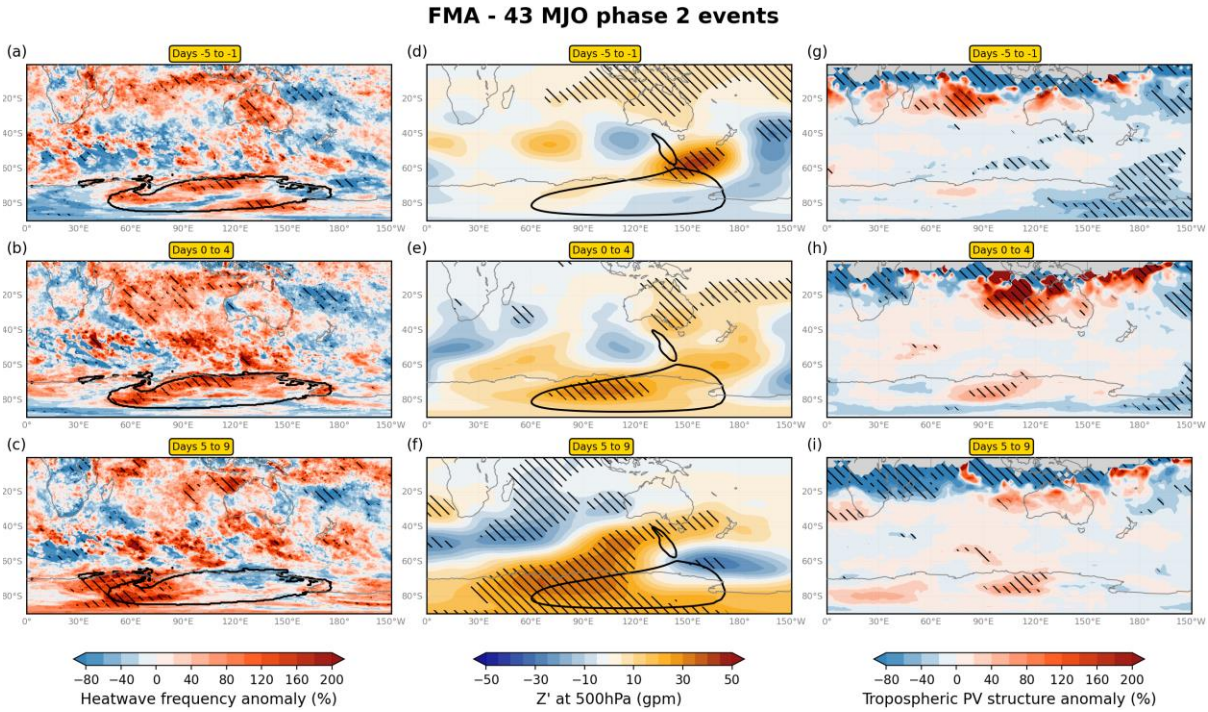

Figure 5. Composites for 43 MJO phase 2 events with a persistence of at least 3 days during February-April (1979-2021) showing anomalies in (a)-(c) heatwave day frequencies (%), (d)-(f) 500-hPa geopotential height (gpm), and (g)-(i) tropospheric PV structure frequencies (%) for a time lag of (a,d,g) -5 to -1 days, (b,e,h) 0 to +4 days, and (c,f,i) +5 to +9 days with respect to the MJO onset day. Hatching indicates statistical significance at a 95% confidence level. Contour lines in (a)-(c) show the locations of heatwave days during 16-23 March 2022, and in (d)-(f) the 500-hPa geopotential height anomalies exceeding 2 standard deviations above normal on 18 March 2022.

The MJO can also influence weather and climate over Antarctica as, for example, demonstrated for an extreme heat event over the Antarctic Peninsula (Rondanelli et al., 2018) and cooling trends over East Antarctica at decadal timescales (Hsu et al., 2021). Wille et al. (2024a) proposed that an active MJO played an important role in the Antarctic heatwave of March 2022 by promoting convection and development of tropical cyclones over the Indian Ocean, which, in turn, contributed to increased moisture transport and Rossby wave propagation into higher latitudes. To further examine the role of enhanced tropical convection over the Indian ocean in heatwave occurrence over East Antarctica, we scrutinize time-lagged composites of heatwave day occurrences and the atmospheric circulation for an active MJO in phase 2, which preceded the Antarctic heatwave of March 2022 (Fig. 4). We observe significant increases in heatwave day occurrences over East Antarctica up to 200% in the two pentads following MJO phase 2 (Fig. 5b,c). The atmospheric circulation exhibits poleward-eastward

Accepted for publication in *Bulletin of the American Meteorological Society.* DOI 10.1175/BAMS-D-23-0141.1.

Rossby wave propagation over the South Indian and southwest Pacific Oceans (Fig. 5e,f), consistent with the findings of previous studies (Henderson et al., 2018; Schwendike et al., 2021), associated with significantly increased poleward RWB into East Antarctica (Fig. 5h,i). Thus, we show here for the first time a significant climatological association between an active MJO over the Indian Ocean and heat extremes and poleward wave breaking over East Antarctica.

Extremeness of early 2022 at seasonal timescales

Next, we analyze the extremeness of the surface weather and atmospheric circulation at seasonal timescales to identify large-scale circulation patterns that may have favored the occurrence of the extreme weather events. In early 2022, eastern-southeastern Australia and southeastern South Africa received more than twice as much precipitation than during the average February-April season (Fig. 6a). Moreover, large parts of these regions received record-breaking seasonal precipitation amounts according to reanalysis-based estimates for the period of 1959-2022 (Fig. 6a). These estimates are in line with station-based measurements showing that annual precipitation amounts in the year 2022 reached the 90th decile over much of eastern Australia and broke records in portions around Brisbane since measurements started in 1900 (Gillett et al., 2023a; Reid et al., 2025). In East Antarctica, a substantial portion of the region between 90-160°E experienced more than three times as many heatwave days compared to the February-April average, including a record-breaking number of heatwave days over the interior of East Antarctica (Fig. 6a). While the studied extreme events undoubtedly contributed to the extremeness of the surface weather at seasonal timescales, we show that all three regions of interest experienced record-breaking surface weather in early 2022 at seasonal timescales.

Previous studies have shown that specific synoptic-scale weather systems can contribute to extreme surface weather at seasonal timescales (Sprenger et al., 2017; Boettcher et al., 2023), including extremely wet seasons (Flaounas et al., 2021). In line with the analysis put forward in this study, we examine the seasonal circulation patterns and synoptic-scale processes that contributed to the extremeness of the surface weather in early 2022. To the south of Australia, we find a positive 500-hPa geopotential height and sea level pressure anomaly, centered near New Zealand and extending westward over the southeastern Indian Ocean (Fig. 6b). In contrast, negative anomalies arise in 500-hPa geopotential height over eastern Australia and in

Accepted for publication in *Bulletin of the American Meteorological Society.* DOI 10.1175/BAMS-D-23-0141.1.

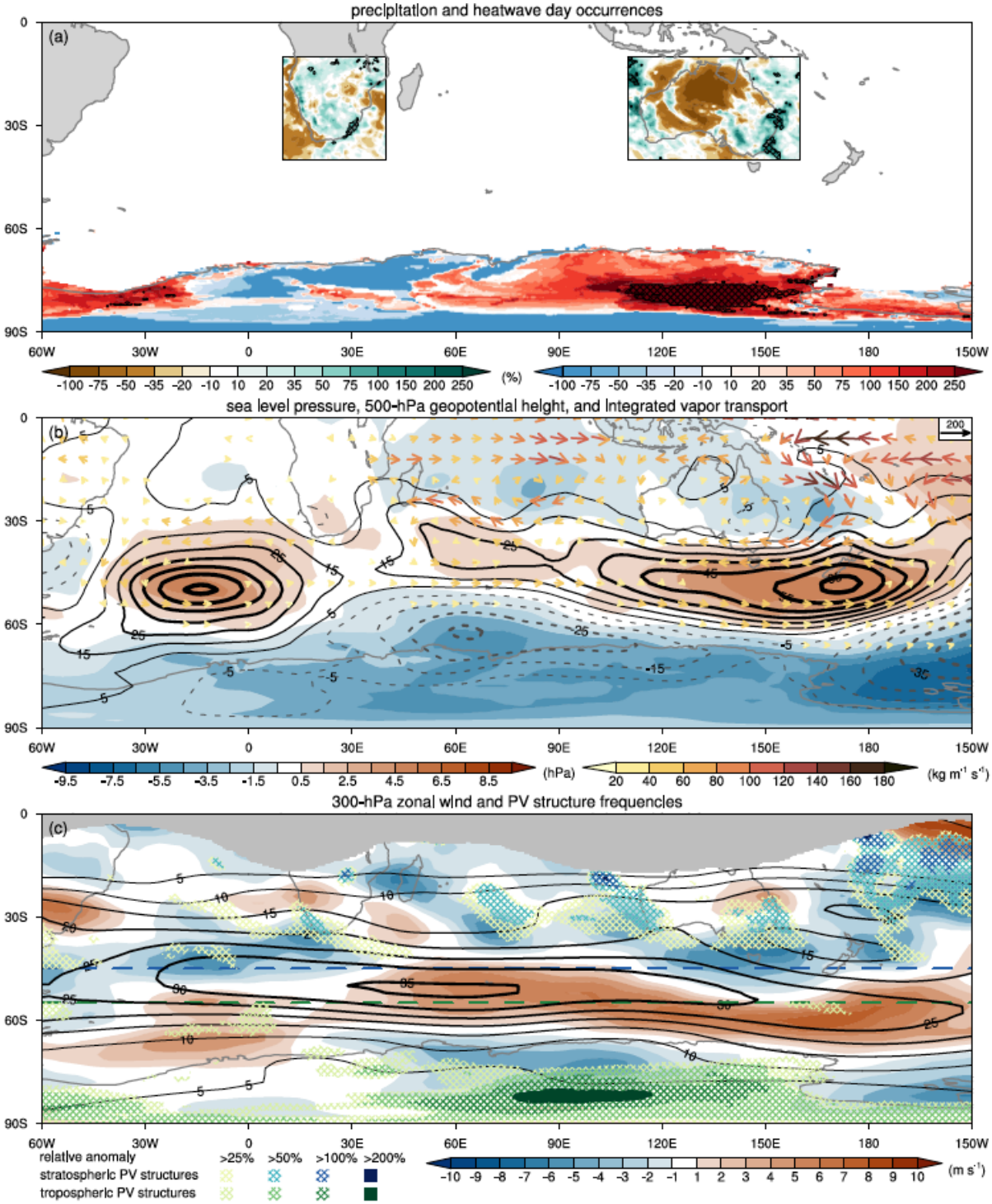

Figure 6. Seasonal anomalies in (a) surface weather and (b,c) the atmospheric circulation for February-April 2022 from climatology (1959-2022). In (a) relative anomalies in seasonal precipitation amounts over Australia and South Africa and in heatwave days over the Antarctic continent whereby black hatching depicts record-breaking values. In (b) anomalies of sea level pressure (hPa) in colors, 500-hPa geopotential height (gpm) in solid black contours for positive values and in dashed grey contours for negative values at 10 gpm intervals starting at 5 gpm, and IVT (kg m^{-1} s^{-1}) in vectors whereby the colors reflect their magnitude, only shown where exceeding 20 kg m^{-1} s^{-1}. In (c) 300-hPa mean zonal wind in black contours and its anomalies in colors (m s^{-1}), and relative anomalies in stratospheric and tropospheric PV structure frequencies north of 45°S and south of 55°S, respectively, in hatching (%), see the legend, shown for positive values only. Regions where climatological stratospheric PV structure frequencies fall below 0.1% are masked grey.

Accepted for publication in *Bulletin of the American Meteorological Society.* DOI 10.1175/BAMS-D-23-0141.1.

sea level pressure off the east Australia coast, suggestive of increased midlatitude upper-level troughs and east coast lows, respectively (Fig. 6b). The combination of the extratropical anticyclonic and subtropical cyclonic circulation anomalies set up an anomalous easterly flow, strengthening the eastward directed atmospheric moisture transport by up to 70 kg m^{-1} s^{-1} (Fig. 6b). In the upper troposphere, we find reduced zonal winds over the southeastern coast of Australia and strengthened zonal winds farther to the south over the Southern Ocean, demonstrating a poleward shifted midlatitude jet (Fig. 6c). The poleward displaced jet is linked to increased RWB frequencies on the equatorward flank of the jet by more than 50% compared to average February-April conditions (Fig. 6c). Thus, the extratropical anticyclonic circulation anomaly and poleward displaced midlatitude jet in combination with increased equatorward RWB frequencies and strengthened easterly moisture transport towards the coast contributed to the extremely wet season over southeastern-eastern Australia in early 2022.

South Africa experienced a very similar configuration of large-scale circulation anomaly patterns as eastern Australia, although the strength of the anomalies was somewhat weaker, likely related to a stronger month-to-month variability of the large-scale circulation in this sector during the early 2022 season (Fig. B4). Over the South Atlantic, we observe positive 500-hPa geopotential height and sea level pressure anomalies (Fig. 6b), largely stemming from a very strong anticyclonic circulation anomaly in April 2022, imposing weak anomalous southeasterly moisture transport towards South Africa (Fig. B4f). Importantly, as for the Australian region, we note a poleward displaced midlatitude jet in the South Atlantic sector, going along with increased equatorward RWB frequencies, ranging from 25% above climatology over the southeastern coast of South Africa to over 50% over its southwest coast (Fig. 6c). This atmospheric configuration is in line with previous studies showing that ridge building over the South Atlantic is associated with RWB, cutoff-low formation, and precipitation over South Africa (Ndarana and Waugh, 2010; Ndarana et al., 2020, 2023; Ivanciu et al., 2023).

Switching focus to East Antarctica, we note an intensified and eastward extended midlatitude jet over the East Indian Ocean sector during February-April 2022 (Fig. 6c), manifesting particularly during the month of March (Fig. B4h). Poleward of the intensified jet, westerly winds are substantially weakened over East Antarctica, inducing favorable conditions

Accepted for publication in *Bulletin of the American Meteorological Society.* DOI 10.1175/BAMS-D-23-0141.1.

for amplifying and breaking waves into polar latitudes (Woollings et al., 2022). Accordingly, poleward RWB frequencies during the early 2022 season were increased by more than 25% over the larger part of East Antarctica, exceeding three times (>200%) the climatological mean frequencies over the interior of the continent (Fig. 6c).

The influence of La Niña

The extreme surface weather in early 2022 across all three regions of interest pose the question whether El Niño Southern Oscillation (ENSO) was linked to the extremeness of the early 2022 season. ENSO was for the 2nd consecutive year in its cold phase, La Niña. The Nino3.4 index (see Appendix A), normally reaching its largest anomaly in December that then reduces during austral autumn, remained amplified until May 2022 (Fig. B5). Previous studies showed that La Niña is associated with increased precipitation totals, extreme precipitation, and flooding over eastern Australia and southern Africa during traditionally defined seasons (King et al. 2014; Ward et al., 2014; Hoell et al., 2015; Sun et al., 2015; McKay et al., 2023; Dao et al., 2023; Huang et al. 2024). Indeed, during La Nina conditions in February-April, precipitation shows a weak increase up to 20% over the east Australian and southeast South African coasts (Fig. 7a). Additionally, heatwave day occurrences over a portion of East Antarctica's interior are significantly increased during La Nina by up to 50%, in agreement with the region where the largest heatwave day increases are found in early 2022 (Fig. 7a). Opposing surface weather anomalies between early 2022 and average La Nina conditions, as for example observed over central-north Australia (Fig. 6a, 7a), may be arise from the influence of other climate variability modes and internal variability of the climate system.

Average circulation anomalies during La Nina conditions reveal a striking similarity with the large-scale circulation patterns that dominated the early 2022 season. At extratropical latitudes over the southwestern Pacific and South Atlantic, we observe positive pressure anomalies in the middle and lower troposphere along with a poleward shifted midlatitude jet and increased RWB frequencies on the equatorward side of the jet (Fig. 7b,c). Near Australia we find positive anomalies in the 500-hPa geopotential height and sea level pressure centered near New Zealand, and a negative sea level pressure anomaly to the east of Australia suggestive of increased east coast lows (Fig. 7b). The combination of positive and negative pressure anomalies at extratropical and subtropical latitudes, respectively, strengthen the easterly

Accepted for publication in *Bulletin of the American Meteorological Society.* DOI 10.1175/BAMS-D-23-0141.1.

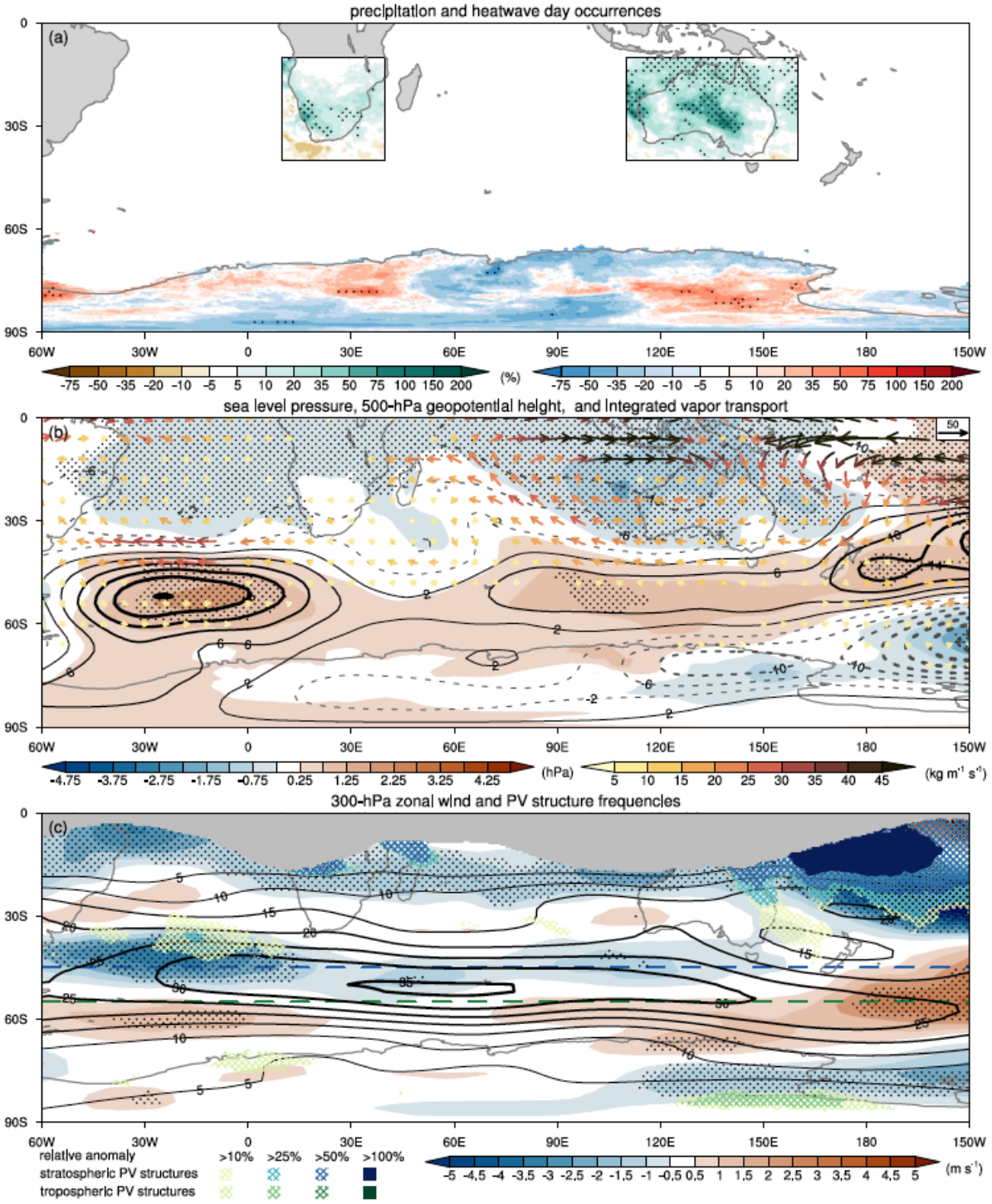

Figure 7. As Fig. 6, but for anomalies during February-April La Nina conditions from climatology (1959-2021). Note that for visibility purposes the color bar scaling is adjusted compared to Fig. 6, with (b) 500-hPa geopotential height contours at 4 gpm intervals starting at 2 gpm. Statistical significance at a 95% confidence level is shown in dots for (a) precipitation amounts and heatwave days, (b) sea level pressure, and (c) 300 hPa zonal wind. Relative anomalies of PV structure frequencies in colored hatching are shown for positive values and where considered significant only.

Accepted for publication in *Bulletin of the American Meteorological Society.* DOI 10.1175/BAMS-D-23-0141.1.

atmospheric moisture transport towards the east Australia coast by up to 20 kg m^{-1} s^{-1} (Fig. 7b). Furthermore, the poleward shifted midlatitude jet to the south of Australia goes along with reduced westerly winds over eastern Australia and increased equatorward RWB frequencies over east Australia's coast ranging from 10% over its southeastern portion to over 50% over its northeastern territories (Fig. 7c). This finding complements previous research showing how ENSO modulates Australian weather during the cool season, including the roles of cyclones, anticyclones, and cutoff lows (Hauser et al., 2020; Grossfeld et al., 2021; Gillett et al., 2023b).

To the southwest of South Africa, we discern a strong anticyclonic circulation anomaly in the middle and lower troposphere during La Niña conditions (Fig. 7b), resembling the strong anticyclonic circulation anomaly as found for April 2022 when the South Africa flooding took place. Consistent with this circulation anomaly, we find a poleward displaced midlatitude jet over the South Atlantic along with increased equatorward RWB frequencies confined to the central part of the South Atlantic during the February-April season (Fig. 7c). During the month of April reduced westerly winds extend eastward over South Africa's coast along with a marginal increase in equatorward RWB frequencies over its southeastern coast exceeding 10% above average April conditions (Fig. B6i). These findings are consistent with previous work showing that, during La Niña conditions, the midlatitude jet is displaced poleward (Hart et al., 2018) and that cutoff-low frequencies, peaking during austral autumn (MAM), are increased (Singleton and Reason, 2007; Favre et al., 2013).

Over East Antarctica, the poleward displaced midlatitude jet occurs in combination with reduced westerlies farther poleward and increased poleward RWB frequencies exceeding 25% above average February-April conditions over a small portion of the continent's interior (Fig. 7c). This suggests that La Nina conditions favor heatwave occurrences over this part of Antarctica associated with poleward RWB.

Conclusions and recommendations for future research

This study was motivated by the occurrence of the exceptionally extreme weather events that struck the Southern Hemisphere within a 2-month period in early 2022. Australia and South Africa incurred unprecedented flood impacts from the end of February until the end of

Accepted for publication in *Bulletin of the American Meteorological Society.* DOI 10.1175/BAMS-D-23-0141.1.

March and mid-April, respectively, while Antarctica experienced a heatwave in mid-March breaking regional and global temperature anomaly records. Our collaborative effort investigated the atmospheric processes leading to these extreme events ranging from local to planetary scales. Our multiscale analysis reveals how climate variability modes on intraseasonal and interannual timescales shaped large-scale circulation patterns that promoted synoptic-scale processes contributing to the formation of the extreme weather events. We conclude this article by highlighting the most important findings and by giving recommendations for future research directions.

Despite the different weather types and geographical locations, all three extreme weather events share the commonality that they result from extratropical Rossby wave breaking (RWB). The east Australia and South Africa flooding resulted from RWB on the equatorward side of the midlatitude jet, consistent with previous studies linking RWB to extreme precipitation over subtropical regions (Barnes et al., 2021, 2023; De Vries, 2021, De Vries et al., 2024; Jin et al., 2024). While previous studies suggested that RWB in a poleward direction from the midlatitude jet can shape polar weather by steering moist air intrusions into the Arctic (Woods et al., 2013; Liu and Barnes, 2015), we show here for the first time that RWB can be of direct relevance to polar heatwaves as demonstrated for the Antarctic heatwave of March 2022. Previous studies investigating the role of weather systems in the occurrence of Arctic heat extremes and melt events focused primarily on cyclones, anticyclones, and atmospheric rivers (Tedesco et al., 2016; Messori et al., 2018; Wernli and Papritz, 2018; Preece et al., 2022, Schmid et al., 2023). Likewise, recent studies addressing the atmospheric drivers of heat extremes, surface melt, and extreme precipitation in Antarctica focused predominantly on the role of atmospheric rivers and, to some lesser extent, on cyclonic and anticyclonic circulation patterns (Welker et al., 2014; Turner et al., 2022; Wille et al., 2019, 2022; Orr et al., 2023; Baiman et al., 2024; Simon et al., 2024). Interestingly, Hepworth et al. (2022) found that a large fraction of Antarctic heat and moisture extremes were neither associated with atmospheric rivers nor cyclones, suggesting the importance of other weather systems in the formation of these surface weather extremes (Siegert et al. 2023). Given the prominent role of poleward RWB in the Antarctic heatwave of March 2022, future research may investigate the contribution of this atmospheric process to the formation of weather extremes in both polar regions.

Accepted for publication in *Bulletin of the American Meteorological Society.* DOI 10.1175/BAMS-D-23-0141.1.

Going beyond process-based considerations, we argue that the accurate simulation of breaking Rossby waves in weather and climate models is important for reliable predictions of extreme weather events. Early warnings for flood hazards in subtropical regions, such as Australia and South Africa, may benefit from diagnosing wave breaking characteristics in medium-range to (sub)seasonal predictions based on the demonstrated predictability of RWB variability from SST forcing (Zhang et al., 2021). Regarding climate projections, Blanchard-Wrigglesworth et al. (2023) showed that a widely used climate model large ensemble fails to accurately simulate extremely large temperature anomalies as observed during the Antarctic heatwave of March 2022 due to biases in the large-scale circulation variability. Moreover, earlier studies reported relatively large biases in wave breaking frequencies in subtropical latitudes in a climate model (Béguin et al., 2013) and substantial inter-model differences in the latitudinal distribution of wave breaking characteristics related to the position of the midlatitude jet (Barnes and Hartmann, 2012). Accordingly, evaluating the fidelity of climate models in simulating wave breaking characteristics and their relation to surface weather is a prerequisite for deriving robust projections of future weather extremes, which is particularly important for regions where these extremes can have disproportionate impacts on society and the environment.

The extreme precipitation events over eastern Australia and South Africa were accompanied by circulation patterns with relatively weak departures from climatology and relatively long durations. This suggests that the extreme precipitation formed under the influence of slow-moving synoptic-scale weather systems favoring the development and maintenance of convective storms over confined regions (Barnes et al., 2023; Reid et al., 2025). In contrast, the Antarctic heatwave of March 2022 was not only very extreme in terms of near-surface air temperatures, but also regarding the atmospheric dynamic and thermodynamic conditions. Local anomalies in 500-hPa geopotential height exceeded 5 standard deviations above normal conditions and atmospheric water content surpassed previous levels of extremeness across the entire Antarctic continent since 1979, exceeding 15 standard deviations above normal. Increasing near-surface air temperatures and warm extremes over the interior of East Antarctica (Turner et al., 2021; Li et al., 2022; Xin et al., 2023) can potentially hold an explanation as to why the standardized anomalies in atmospheric moisture content were so large given that fractional changes in saturation specific humidity are larger in very cold conditions compared to warmer temperature regimes. Further research may investigate the

Accepted for publication in *Bulletin of the American Meteorological Society.* DOI 10.1175/BAMS-D-23-0141.1.

influence of climate change on Antarctic weather extremes and their driving atmospheric processes, which will become increasingly important in the future given the potentially large impacts of Antarctic changes on the global climate system (Siegert et al. 2023).

Based on a systematic climatological analysis, we infer that all three extreme events are associated with a remote influence of tropical atmospheric variability at intraseasonal to interannual timescales. At intraseasonal timescales, we find that both flood episodes over eastern Australia at the end of the months February and March were preceded by enhanced tropical convection over the eastern Indian Ocean and the Maritime Continent (MJO phases 3 and 4). A climatological analysis confirms a weak linkage between these MJO phases and increased precipitation over eastern Australia and the associated circulation patterns, in line with previous work (Wheeler et al., 2009; Dao et al. 2023; Cowan et al., 2023). The South Africa flooding was preceded by a weak MJO (amplitude < 1) in phase 6 and 7 during 9-13 April, and thus, we cannot rule out a possible influence of the MJO on this event. Furthermore, we find a strong linkage between enhanced tropical convection over the Indian Ocean and heatwaves over East Antarctica. A strong MJO phase 2 not only preceded the Antarctic heatwave of March 2022 (Wille et al. 2024a) but is also generically linked to heat extremes over East Antarctica associated with poleward-eastward propagating Rossby wave trains over the extratropical Indian Ocean and poleward wave breaking into East Antarctica.

At interannual timescales, we found that La Niña is associated with anticyclonic circulation anomalies in low midlatitudes over the South Atlantic and southwestern Pacific along with a poleward displaced midlatitude jet, increased RWB frequencies on the equatorward side of the jet, and strengthened easterly atmospheric moisture transport towards the east-southeast Australian and southeast African coasts. Both regions experienced extremely wet seasons in early 2022 with record-breaking precipitation amounts in some parts of these regions. In the southwestern Pacific, an anomalous anticyclonic circulation dominated from February to April 2022, and is part of the Pacific-South America pattern wave train that has been linked to La Nina (Irving and Simmonds, 2016). In the South Atlantic, the strong anomalous anticyclonic circulation developed during April and is typical of La Nina conditions too (Fig. 7b). Our findings also suggest that La Niña is associated with significantly increased heatwave days over a part of East Antarctica's interior. Future research may include the influence of other

Accepted for publication in *Bulletin of the American Meteorological Society.* DOI 10.1175/BAMS-D-23-0141.1.

climate variability modes on the discussed types of surface weather extremes and atmospheric circulation patterns. For example, east Australia wet conditions have been linked to a positive phase of the Southern Annular Mode (Holgate et al., 2022; Boschat et al. 2023), and at decadal timescales, ENSO's influence on Australian weather is strengthened during a negative phase of the Interdecadal Pacific Oscillation (King et al., 2013; McKay et al., 2023).

We emphasize that the three extreme weather events, although sharing commonalities, were not directly linked to another as they occurred in different regions in different periods and resulted from different individual weather systems. We argue that the three extreme weather events resulted from individual synoptic-scale processes, specifically the breaking of extratropical Rossby waves, favored by remote tropical weather and climate variability on intraseasonal to interannual timescales. The extremeness of the events may have been further amplified by climate warming, particularly its thermodynamic influence (Pinto et al., 2022; King et al., 2023). Future research may disentangle the roles of weather, climate variability, and climate change in the occurrence of extreme weather events with high impacts on society and the polar cryosphere in the Southern Hemisphere.

Accepted for publication in *Bulletin of the American Meteorological Society.* DOI 10.1175/BAMS-D-23-0141.1.

Acknowledgments.

We thank Marcia Zilli (University of Oxford) and Edwin Gerber (New York University) for helpful discussions.

Data Availability Statement.

All datasets used in this study are freely available from the respective data providers. ERA5 reanalysis data from the ECWMF were obtained via the MARS archive. SSTs from the Extended Reconstructed Sea Surface Temperature dataset version 5 (ERSSTv5) were retrieved from the NCAR research data archive (https://rda.ucar.edu/). Societal impacts from natural disasters in Australia and South Africa were used from the Emergency event database (EM-DAT) via https://www.emdat.be, accessed on 24-05-2024. Output data from applied diagnostics, as detailed in Appendix A, can be provided by the authors upon request.

Accepted for publication in *Bulletin of the American Meteorological Society.* DOI 10.1175/BAMS-D-23-0141.1.

APPENDIX A

Data and diagnostics

This appendix details the data and diagnostics used in this study.

Data

All diagnostics have been applied to the ERA5 reanalysis data (Hersbach et al. 2022) except for sea surface temperature for calculating the Niño3.4 index for which we used ERSSTv5 (Huang et al. (2017). In addition, for precipitation timeseries in Fig. B1, we use satellite-based estimates from GPM IMERG (Huffman et al., 2020) to provide complementary perspective on precipitation. We emphasize that reanalysis-based precipitation as used in this study, both precipitation amounts and return periods, should be interpretated with caution and as a rough estimate of precipitation, particularly values based at local scales (i.e., single grid points).

Return periods of daily precipitation extremes

We compute return periods (RPs) to quantify the rareness of days with heavy precipitation. Using RPs, we can compare the rareness of heavy precipitation days for each grid point over a large domain with a spatially varying climatology. To obtain RPs, we first fit the seasonal precipitation distribution for each grid point in a box over eastern Australia (120E-170E, 5S-50S) and South Africa (0-50E, 5S-50S). We then compute the quantile associated with each precipitation day.

We fit the precipitation distribution with the extended generalized Pareto distribution (EGPD, Tencaliec et al., 2020). We thereby model the probability distribution of daily precipitation greater than 1 mm day^{-1}. The EGPD follows extreme value properties for both upper tail and lower tail, while providing a distribution model for the entire distribution of precipitation. The advantage of the EGPD is its capacity to model the whole range of the precipitation distribution. We can therefore compute a return period for each day with precipitation, with a sound modeling of the heavy precipitation probabilities and without having to select a threshold for extreme events. We perform the fitting of the EGPD seasonally (MAM, JJA, SON, DJF), with Bernstein polynomials of degree 10. For each season, we discard grid points that have less than 100 days with precipitation greater than 1 mm day^{-1}.

Accepted for publication in *Bulletin of the American Meteorological Society.* DOI 10.1175/BAMS-D-23-0141.1.

For a daily precipitation x > 1mm, we calculate the associated quantile q with the fitted distribution:

$$q = \mathbb{P}[X \leq x] \qquad (1)$$

with X the precipitation distribution for the corresponding grid point and season. From the quantile q, we can estimate the associated return period T (in years):

$$T = \frac{1}{(1-q)n_{wet\ days\ per\ seas}} = \frac{n_{years}}{(1-q)n_{wet\ days}} \quad (2)$$

where $n_{wet\ days\ per\ seas}$, the number of days per season with precipitation greater than 1 mm day^{-1}, is calculated as $\frac{n_{wet\ days}}{n_{years}}$, where $n_{wet\ days}$ is the total number of days per season with precipitation greater than 1 mm day^{-1} over the period 1979-2022 and n_{years} = 44 years.

The obtained return period T associated with the daily precipitation x is the estimated average time between precipitation events of intensity x or greater.

The return period values can be sensitive to the specific choices, such as the degree of Bernstein polynomials and the period used for the fitting. We provide return periods as an illustration of the extremeness rather than a strict measure.

Heatwave index

We identify the occurrence and intensity of heatwaves over Antarctica based on ERA5 reanalysis data for the period 1959-2022. We define heatwaves as at least 3 consecutive days with temperatures exceeding a given threshold. Following Russo et al. (2015), Perkins et al. (2020), and Russo and Domeisen (2023), this threshold (Tr90), is calculated as the 90th percentile of daily maxima of hourly 2m air temperatures in a sliding window of 30 days centred on the considered day of a year, over the 30-year reference period of 1981-2010. Following Russo et al. (2015), for a given day d, let us consider the set of data A_d defined by

$$A_d = \cup_{y=1981}^{2010} \cup_{i=d-15}^{d+15} T_{y,i} \qquad (3)$$

where y varies over the years of the reference period, i over the 30-day sliding window around the selected day d, and T represents daily maximum temperatures. We then define the threshold Tr90 as the 90th percentile of A_d.

Accepted for publication in *Bulletin of the American Meteorological Society.* DOI 10.1175/BAMS-D-23-0141.1.

Our main goal here is to compare the intensity of heatwaves occurring across Antarctica during different seasons. For this reason, we use a standardized metric, allowing to compare events occurring at different locations and different times of the year. For each day d identified as heatwave, we first define the heatwave maximum temperature anomalies as:

$$T'_d = T_d - Tr90 \qquad (4)$$

where T_d is the daily maximum temperature on the considered day d of a heatwave. Then, if we define the total number of heatwave days occurring over the reference period 1981-2010 as $nHWday_{1981–2010}$, we can calculate the standardized heatwave intensity I_d for the same day d as:

$$I_d = \frac{T'_d}{Median\left(\cup_{i=1}^{nHWday_{1981-2010}} T'_i\right)} \qquad (5)$$

where the denominator represents the median value of the anomalies of daily maximum temperatures calculated over all the heatwave days of the reference period.

Finally, the intensity of a given heatwave h is given simply by the sum of I_d over all consecutive heatwave days of the event h:

$$HWI_h = \sum_{d=1}^{nHWday_h} I_d \qquad (6)$$

Extremeness of the atmospheric conditions

To quantify the extremeness of the atmospheric conditions during the three extreme events, we compute the departure from climatology of several atmospheric variables, including the 500-hPa geopotential height, total column water, and the zonal and meridional components of IVT. For each of these variables, we compute standardized anomalies using 21-day running mean and standard deviation values of daily means centered on the day in question to account for spatially and seasonally varying climatology (after Hart and Grumm, 2001; De Vries et al., 2016, 2018; De Vries, 2021):

$$N = \frac{(X-\mu)}{\sigma}, \qquad (7)$$

Where X is the daily mean value of the variable, μ the climatological mean, and σ the standard deviation of daily mean values within the 21-day running window using a reference period of 1979-2022.

Rossby wave breaking

Accepted for publication in *Bulletin of the American Meteorological Society.* DOI 10.1175/BAMS-D-23-0141.1.

To diagnose RWB, we identify elongated and separated structures in PV contours, so-called PV streamers and PV cutoffs, following the approach introduced by Wernli and Sprenger (2007). In addition, we incorporate modifications for the identification of PV streamers by Sprenger et al. (2013), De Vries et al. (2018, 2024) and De Vries (2021), and for PV cutoffs, by Skerlak et al. (2014) and Portmann et al. (2021). We compute PV from horizontal wind and temperature fields on model levels and then interpolate PV at isentropic surfaces between 275 and 360 K with 5 K intervals. To identify PV streamers and cutoffs, hereafter PV structures, we use the +/-2 potential vorticity unit (PVU) contour (1 PVU = 10^{-6} K kg^{-1} m^2 s^{-1}) representing the dynamical tropopause. PV structures with stratospheric air masses (|PV| > 2 PVU) represent equatorward wave breaking typically observed in regions where tropospheric air masses prevail, and likewise, PV structures with tropospheric air masses (|PV| < 2 PVU) represent poleward wave breaking typically occurring in regions where stratospheric air masses dominate.

For identifying PV streamers and cutoffs, we follow a three-step procedure. First, we determine the stratospheric PV reservoir by the most equatorward +/-2 PVU contour that encircles the globe. If no circumglobal +/-2 PVU is present, we consider the longest +/-2 PVU contour as stratospheric body, provided it spans a zonal distance of more than 180 degrees and reaches at least poleward of 80°N/S. In addition, we remove any stratospheric PV reservoir if it intersects with the Earth's surface or if it does not connect vertically with stratospheric PV reservoirs at isentropic surface aloft to avoid erroneously assigning stable air masses near the surface over the Poles as stratospheric reservoirs. Second, we evaluate each pair of contour points at 2 PVU contours encircling the stratospheric PV reservoirs on the following geometric criteria: (1) the spherical distance (W) < 1500 km, (2) the contour length between the two points (L) > 1000 km, (3) the ratio length over width ($r = L / W$) > 1, and (4) the contour length between the two points (L) < 15,000 km. If stratospheric PV streamers cover more than 50 % of the stratospheric PV reservoir's surface, all PV streamers on that isentropic surface are then removed to avoid spurious PV streamers at isentropic surfaces with heavily distorted 2 PVU contours.

Third, we consider all remaining 2 PVU contours as potential PV cutoffs. Stratospheric PV cutoffs (PV > |2 PVU|) are evaluated on (1) their vertical connection to the stratospheric PV reservoir aloft, including via other partially overlapping stratospheric PV cutoffs on isentropic surfaces above, (2) specific humidity < 0.1 g kg^{-1} and relative humidity < 70 % for at least half of the PV cutoff's surface, and (3) no intersection with the Earth's surface. If any of these

Accepted for publication in *Bulletin of the American Meteorological Society.* DOI 10.1175/BAMS-D-23-0141.1.

conditions are not fulfilled, the stratospheric PV cutoff is removed from the selection to avoid PV features originating from orographic friction or diabatic processes to be classified as PV cutoff from stratospheric origin. Likewise, we evaluate tropospheric PV cutoffs (1) on their presence underneath the stratospheric reservoir, allowing for structures that are vertically connected with other tropospheric PV cutoffs on isentropic surfaces aloft via partial overlap, and (2) intersections with the Earth's surface. If any of these conditions are not met, the tropospheric PV reservoir is removed with the same purpose of retaining only tropospheric PV cutoffs resulting from RWB and removing structures associated with radiative or frictional processes. Additionally, we only retain stratospheric PV cutoffs with a surface area between 25,000 and 5,000,000 km^2 and for tropospheric PV cutoffs a surface area larger than 25,000 km^2 to focus on synoptic-scale structures. The criterion of stratospheric and tropospheric PV cutoffs being located underneath the stratospheric PV reservoir implies that PV cutoffs can only be detected on isentropic surfaces up to 355K.

The MJO index, composites, and significance testing

We use the daily values of the real-time multivariate MJO (RMM) index (Wheeler and Hendon, 2004) retrieved from the Bureau of Meteorology (http://www.bom.gov.au/climate/mjo/). This index is derived from the combined empirical orthogonal functions of anomalies in upper (200-hPa) - and lower (850-hPa) - tropospheric zonal winds and equatorially average (15°S-15°N) outgoing long-wave radiation. The amplitude of the RMM index is calculated as $RMM = \sqrt{RMM1^2 + RMM2^2}$. The MJO is considered strong or active (weak or inactive) when the amplitude of the MJO is greater (smaller) than 1 (Wheeler and Hendon, 2004, Henderson 2017). The location of the MJO is given by MJO phases. We define MJO events by an RMM amplitude greater than 1 for at least 3 consecutive days in a particular phase. Composites of anomalous surface weather (heatwave day occurrence) and atmospheric circulation (500-hPa geopotential height and tropospheric PV structures) are constructed for time lagged pentads around the onset of each MJO event. Statistical significance is evaluated at the 95% confidence level with a Monte Carlo approach (Martius et al., 2008) whereby a double-sided test is applied on a distribution of 300 samples of randomly selected pentads in February-April. The period is limited to 1979-2021 to exclude a possible influence of the selected extreme weather events occurring in the year 2022.

Nino3.4 index, La Nina composites, and significance testing

Accepted for publication in *Bulletin of the American Meteorological Society.* DOI 10.1175/BAMS-D-23-0141.1.

We calculate the Nino3.4 index from SST anomalies using monthly data from the Extended Reconstructed Sea Surface Temperature dataset version 5 (ERSSTv5), as described by Huang et al. (2017). We average SSTs over the region from 5°N to 5°S and from 170°W to 120°W. Following the approach by Casselman et al. (2021), we filter out variations in the data at timescales longer than 30 years using a Fast Fourier Transform. SST anomalies using a 3-monthly running average are then assessed against a climatological baseline spanning January 1959 to December 2022.

To construct seasonal and monthly composites of surface weather and atmospheric circulation anomalous during La Niña conditions, we first linearly detrend the fields to remove the influence of climate change and to focus on signals arising from interannual variability. Then, we construct composite means based on the seasons and months when the Nino3.4 index falls below -0.5. Statistical significance of the composite mean values is tested using 1000 Monte Carlo samples based on composite means from randomly shuffled seasonal and monthly mean values consistent with the number of seasons and months of the La Nina test statistic. We consider tested values significant at a 95% confidence level, i.e., tested values that fall within the 2.5% lower and upper tails of the null distribution. As for the investigation of the MJO, we limit the period for constructing La Nina composites to 1959-2021 to avoid potential signals arising from the 2022 extreme weather events.

Accepted for publication in *Bulletin of the American Meteorological Society.* DOI 10.1175/BAMS-D-23-0141.1.

APPENDIX B

Supporting figures

This Appendix contains figures that support the findings of the study.

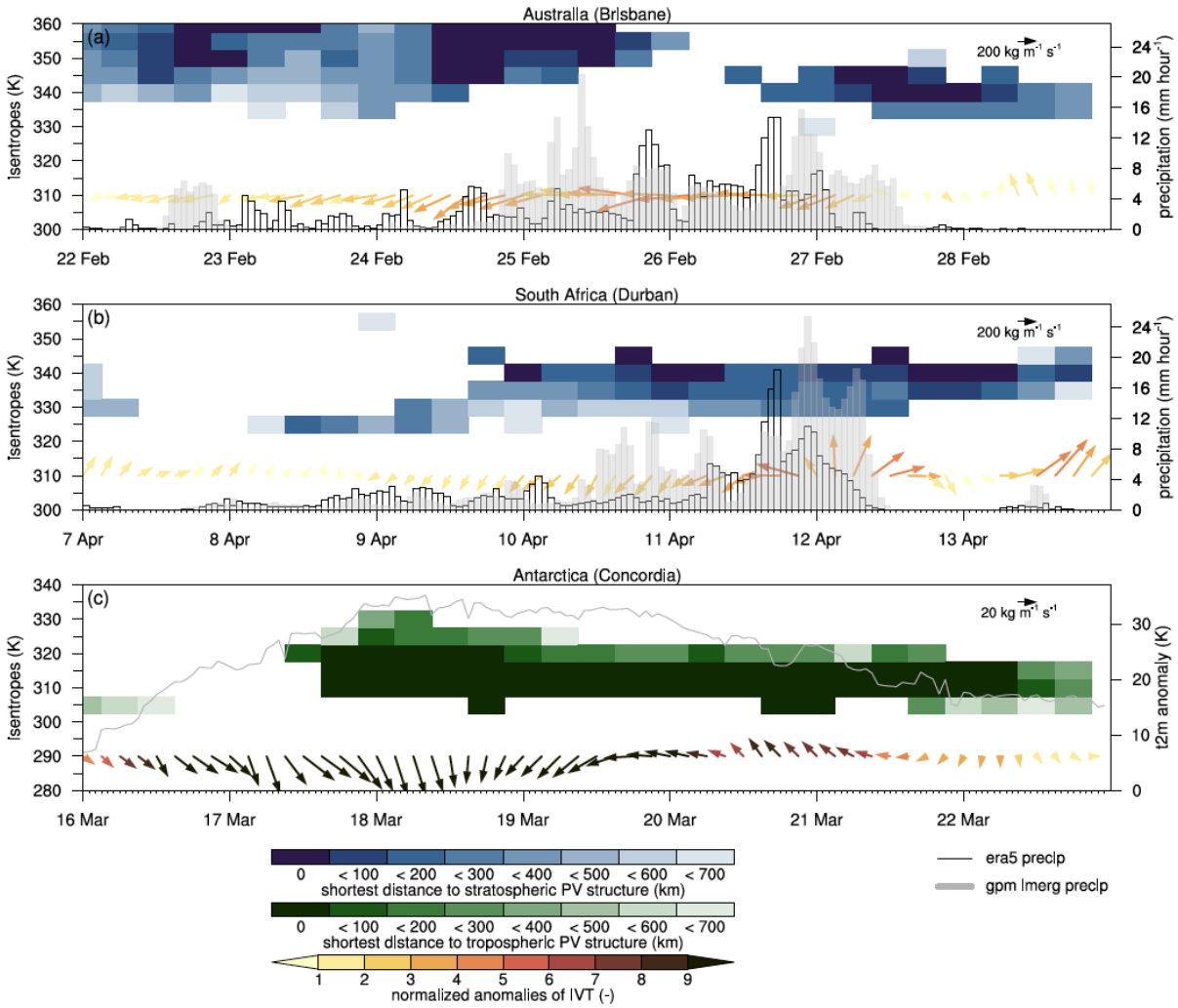

Figure B1. The time evolution of surface weather and synoptic-scale processes from a local perspective. In (a) hourly precipitation (mm) from ERA5 (black lines) and GPM IMERG (gray shading) at the nearest grid point to Brisbane (153°E, 27.5°S), eastern Australia. In (b), as in (a), but for the nearest grid point to Durban (31.0°E, 29.9°S), South Africa. In (c), as (a), but for hourly ERA5 2m temperature anomalies from the 21-day running mean at the Concordia station (123.3°E, 75.1°S). The blue and green shading depicts the shortest distance (km) from these locations to 6-hourly stratospheric and tropospheric PV structures, representing equatorward and poleward RWB, respectively, in time and vertical direction (isentropic surfaces), and the vectors show, at 3-hourly intervals, the direction and magnitude of the actual IVT (kg m^{-1} s^{-1}) whereby their colors indicate the values of standardized anomalies in zonal and meridional IVT combined.

Accepted for publication in *Bulletin of the American Meteorological Society.* DOI 10.1175/BAMS-D-23-0141.1.

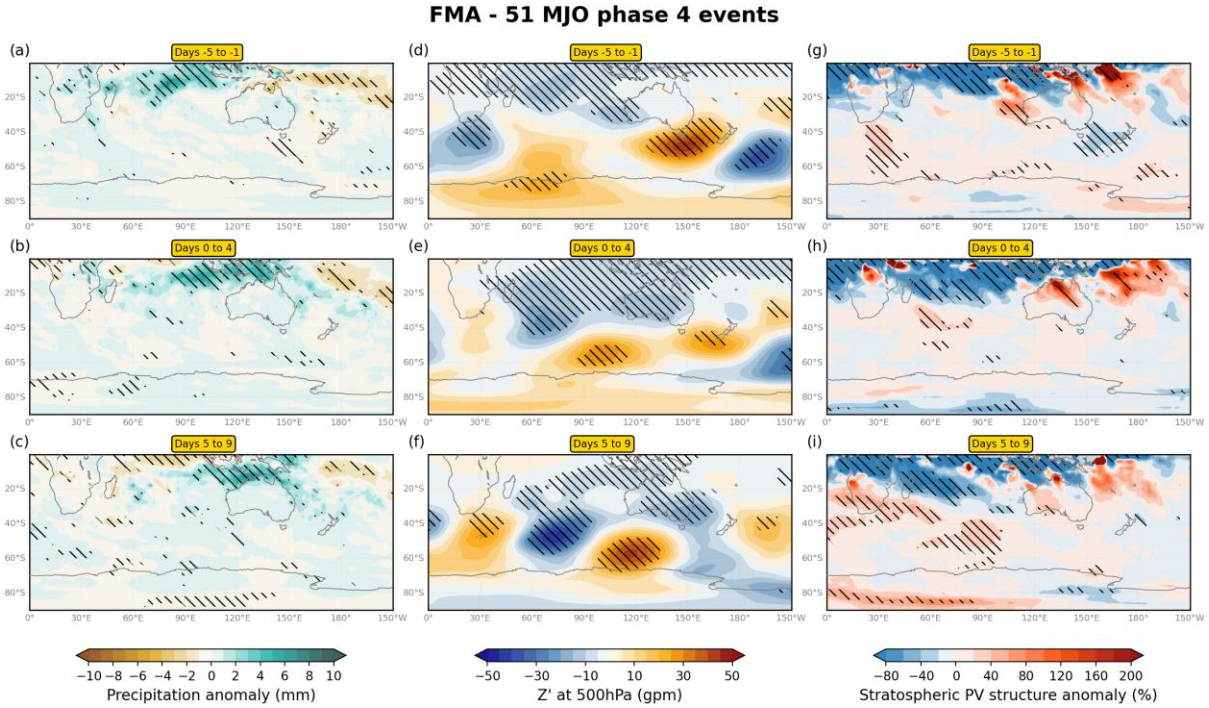

Figure B2. As Fig. 5, but for 51 MJO phase 4 events during February-April showing anomalies in (a)-(c) precipitation amounts (mm), (d)-(f) 500-hPa geopotential height (gpm), and (g)-(i) stratospheric PV structure frequencies (%).

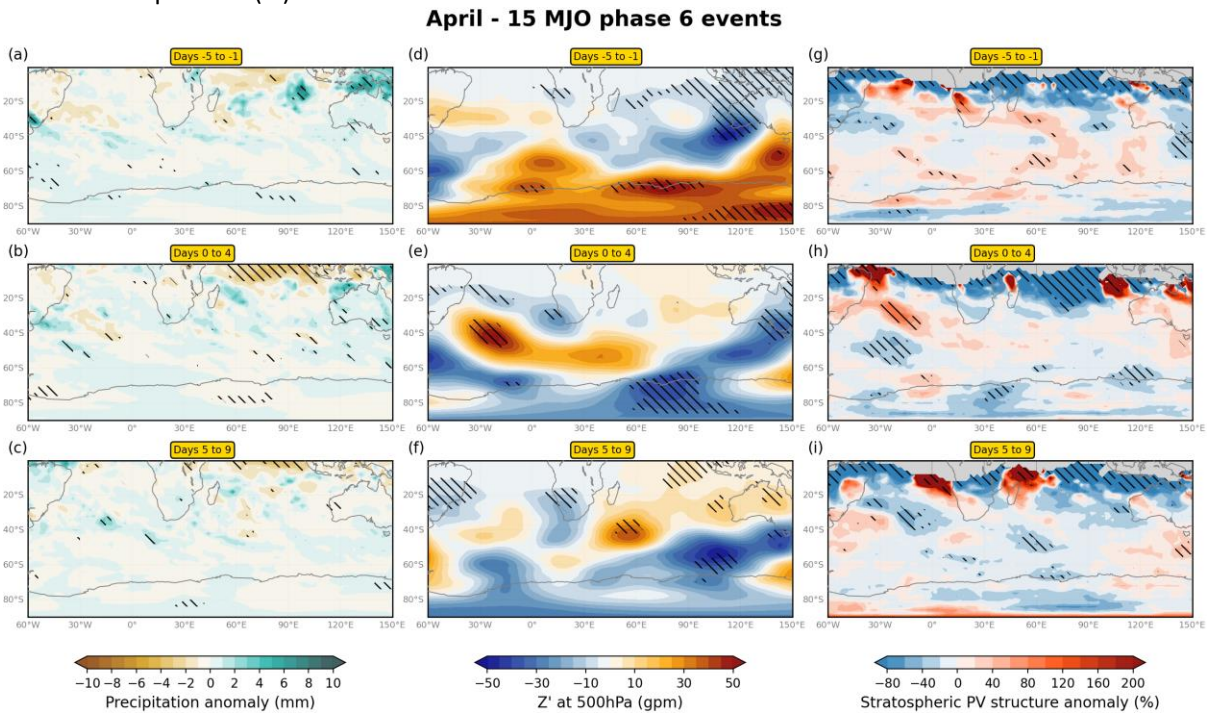

Figure B3. As Fig. B2, but for 15 MJO phase 6 events during April only.

Accepted for publication in *Bulletin of the American Meteorological Society.* DOI 10.1175/BAMS-D-23-0141.1.

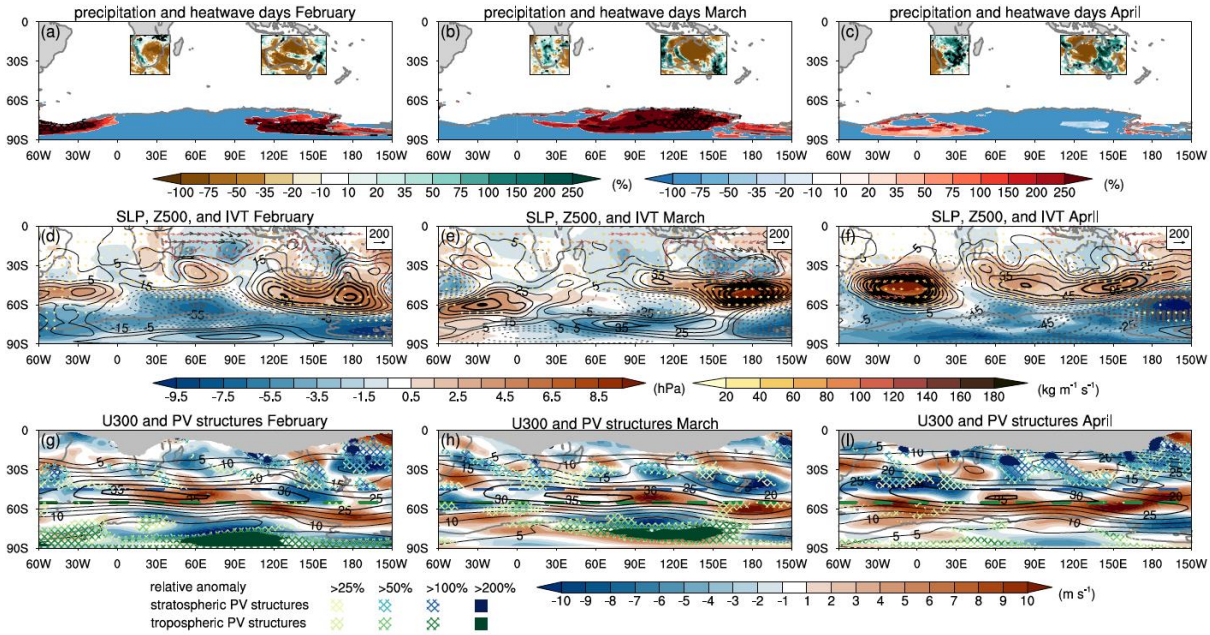

Figure B4. As Fig. 6, but for monthly mean anomalies in (a,d,g) February, (b,e,h) March, and (c,f,i) April 2022 from climatology (1959-2022).

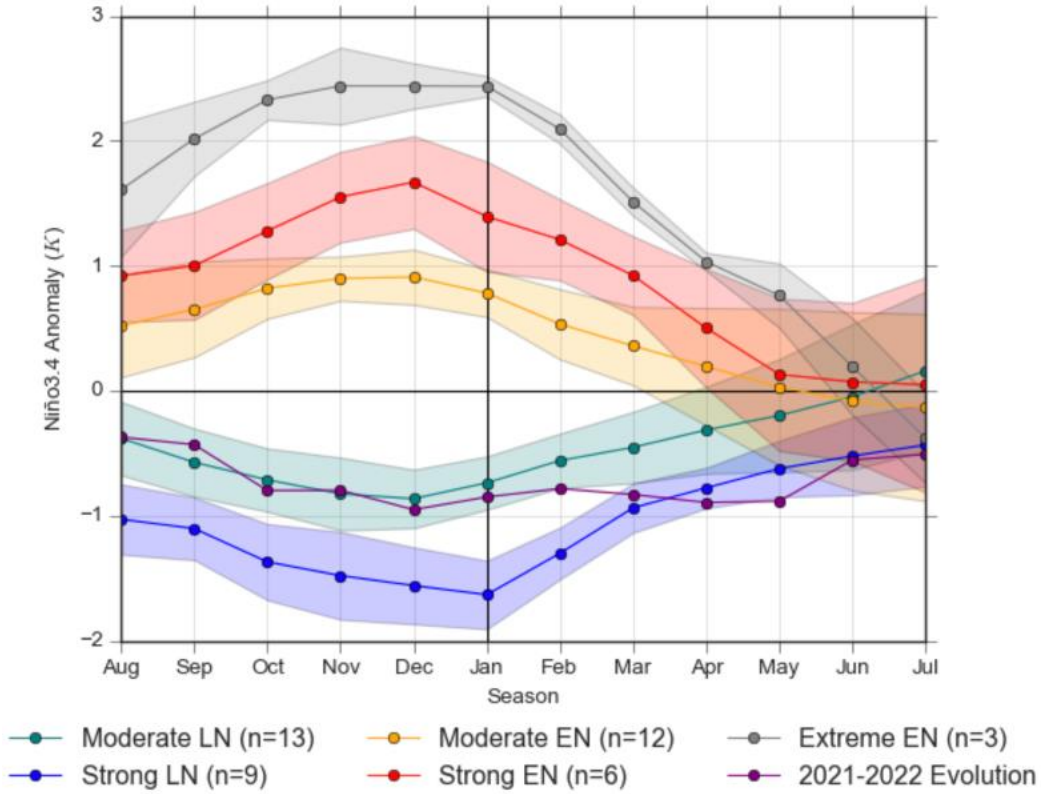

Figure B5. Composited seasonal evolution of the Niño-3.4 index based on SST anomalies that characterize El Niño (EN) and La Niña (LN) events for the period of 1959-2022. ENSO phases are categorized by their strength: moderate (±0.5–1.0 standard deviation [std dev]), strong (±1.0–2.0 std dev), and extreme (>±2.0 std dev, note only extreme El Niño events exist) and the year 2021-2022 is shown in purple. These categorizations are based on the 5-month average of the Niño-3.4 index, specifically during the peak season of October to February (ONDJF), following the methodology introduced by Casselman et al. (2021). The shading in the figure denotes the uncertainty bounds of ±1 std dev. The y-axis quantifies the SST anomalies in Kelvin, showing the intensity of ENSO events.

Accepted for publication in *Bulletin of the American Meteorological Society.* DOI 10.1175/BAMS-D-23-0141.1.

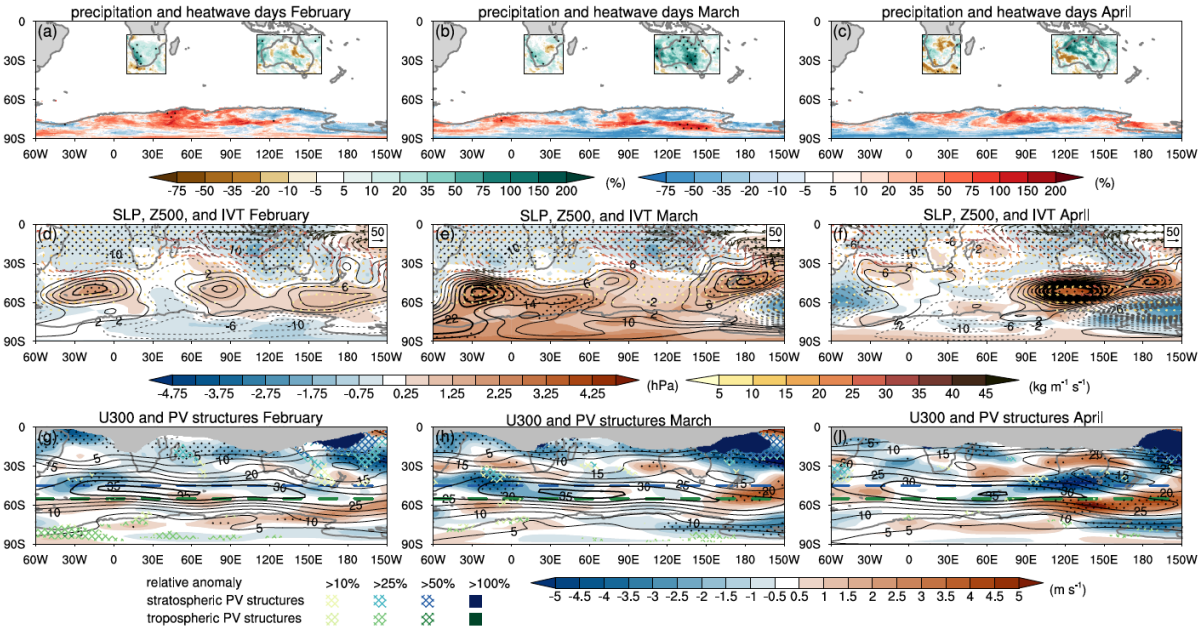

Figure B6. As Fig. 7, but for monthly mean anomalies in (a,d,g) February, (b,e,h) March, and (c,f,i) April for La Niña conditions from climatology (1959-2021).

Accepted for publication in *Bulletin of the American Meteorological Society.* DOI 10.1175/BAMS-D-23-0141.1.

REFERENCES

Alcântara, E., and Coauthors, 2023: Deadly disasters in southeastern South America: flash floods and landslides of February 2022 in Petrópolis, Rio de Janeiro. *Nat. Hazards Earth Syst. Sci.*, **23**, 1157-1175, https://doi.org/10.5194/nhess-23-1157-2023.

Ali, S. M., O. Martius, and M. Röthlisberger, 2021: Recurrent Rossby wave packets modulate the persistence of dry and wet spells across the globe. *Geophys. Res. Lett.*, **48**, e2020GL091452. https://doi.org/10.1029/2020GL091452.

Ali, S. M., M. Röthlisberger, T. Parker, K. Kornhuber, and O. Martius, 2022: Recurrent Rossby waves and south-eastern Australian heatwaves, *Wea. Climate. Dyn.*, **3**, 1139–1156, https://doi.org/10.5194/wcd-3-1139-2022.

Baimann, R., A. C. Winters, B. Pohl, V. Favier, J. D. Wille, and K. R. Clem, 2024: Synoptic and planetary-scale dynamics modulate Antarctic atmospheric river precipitation intensity, *Commun. Earth. Environ.*, 5, 1243, https://doi.org/10.1038/s43247-024-01307-9.

Barnes, E. A., and D. L. Hartmann, 2012: Detection of Rossby wave breaking and its response to shifts of the midlatitude jet with climate change, *J. Geophys. Res. Atmos.*, **117**, D09117, https://doi.org/10.1029/2012JD017469.

Barnes, M. A., K. Turner, T. Ndarana, W. A. and Landmann, 2021: Cape storm: A dynamical study of a cut-off low and its impact on South Africa, *Atmos. Res.*, **249**, 105290, https://doi.org/10.1016/j.atmosres.2020.105290.

Barnes, M. A., M. King, M. Reeder, and C. Jakob, 2023: The dynamics of slow-moving coherent cyclonic potential vorticity anomalies over the eastern seaboard of Australia. *Quart. J. Roy. Meteor. Soc.*, **149**, 2233-2251, https://doi.org/10.1002/qj.4503.

Blanchard-Wrigglesworth, E., T. Cox, Z. I. Espinosa, and A. Donohoe, 2023: The largest ever recorded heatwave—Characteristics and attribution of the Antarctic heatwave of March 2022. *Geophys. Res. Lett.*, **50**, e2023GL104910. https://doi.org/10.1029/2023GL104910.

Béguin, A., O. Martius, M. Sprenger, P. Spichtinger, D. Folini, and H. Wernli, 2013: Tropopause level Rossby wave breaking in the Northern Hemisphere: a feature-based validation of the ECHAM5-HAM climate model, *Int. J. Climatol.*, **33**, 3072-3082, https://doi.org/10.1002/joc.3631.

Accepted for publication in *Bulletin of the American Meteorological Society.* DOI 10.1175/BAMS-D-23-0141.1.

Boettcher, M., M. Röthlisberger, R. Attinger, J. Rieder, and H. Wernli, 2023: The ERA5 extreme seasons explorer as a basis for research at the weather and climate interface. *Bull. Amer. Meteor. Soc.*, **104**, E631–E644, https://doi.org/10.1175/BAMS-D-21-0348.1.

Boschat, G., A. Purich, I. Rudeva, and J. Arblaster, 2023: Impact of zonal and meridional atmospheric flow on surface climate and extremes in the southern Hemisphere. *J. Climate*, **36**, 5041–5061. https://doi.org/10.1175/jcli-d-22-0251.1

Bureau of Meteorology, 2022: Extreme rainfall and flooding in south-eastern Queensland and eastern New South Wales. *Special Climate Statement 76*, 29 pp., http://www.bom.gov.au/climate/current/statements/scs76.pdf?20220525.

Casselman, J. W., A. S. Taschetto, and D. I. V. Domeisen, 2021: Nonlinearity in the pathway of El Niño-Southern Oscillation to the tropical North Atlantic. *J. Climate*, **34**, 7277–7296. https://doi.org/10.1175/jcli-d-20-0952.1.

Cowan, T., M. C. Wheeler, and A. G. Marshall, 2023: The combined influence of the Madden–Julian oscillation and El Niño–Southern Oscillation on Australia rainfall. *J. Climate*, **36**, 313–334, https://doi.org/10.1175/JCLI-D-22-0357.1.

Dao, T. L., C. L. Vincent, T. P. Lane, 2023: Multiscale influences on rainfall in northeast Australia, *J. Climate*, **36**, 5989-6006, https://doi.org/10.1175/JCLI-D-22-0835.1.

De Vries, A., S. Feldstein, M. Riemer, E. Tyrlis, M. Sprenger, M. Baumgart, M. Fnais, and J. Lelieveld, 2016: Dynamics of tropical–extratropical interactions and extreme precipitation events in Saudi Arabia in autumn,winter and spring. *Quart. J.Roy. Meteor. Soc.*, **142**, 1862–1880, https://doi.org/10.1002/qj.2781.

De Vries, A. J., H. G. Ouwersloot, S. B. Feldstein, M. Riemer, A. M. E. Kenawy, M. F. McCabe, and J. Lelieveld, 2018: Identification of tropical-extratropical interactions and extreme precipitation events in the Middle East based on potential vorticity and moisture transport. *J. Geophys. Res. Atmos.*, **123**, 861–881, https://doi.org/10.1002/2017JD027587.

De Vries, A. J., 2021: A global climatological perspective on the importance of Rossby wave breaking and intense moisture transport for extreme precipitation events. *Wea. Climate. Dyn.*, **2**, 129-161, https://doi.org/10.5194/wcd-2-129-2021.

De Vries, A. J., M. Armon, K. Klingmüller, R. Portmann, M. Röthlisberger, and D. I. V. Domeisen, 2024: Breaking Rossby waves drive extreme precipitation in the world's arid

Accepted for publication in *Bulletin of the American Meteorological Society.* DOI 10.1175/BAMS-D-23-0141.1.

regions. *Comm. Earth Environ.*, **5**, 493, https://www.nature.com/articles/s43247-024-01633-y

Dowdy, A. J., and Coauthors, 2019: Review of Australian east coast low pressure systems and associated extremes. *Climate Dyn.*, **53**, 4887–4910, https://doi.org/10.1007/s00382-019-04836-8.

Favre, A., B. Hewitson, C. Lennard, R. Cerezo-Mota, and M. Tadross, 2013: Cutoff lows in the South Africa region and their contribution to precipitation. *Climate Dyn.* **41**, 2331–2351, DOI10.1007/s00382-012-1579-6.

Flaounas, E., M. Röthlisberger, M. Boettcher, M. Sprenger, and H. Wernli, 2021: Extreme wet seasons – their definition and relationship with synoptic-scale weather systems. *Wea. Climate Dyn.*, **2**, 71–88, https://doi.org/10.5194/wcd-2-71-2021.

Fragkoulidis, G., V. Wirth, P. Bossmann, and A. Fink, 2018: Linking Northern Hemisphere temperature extremes to Rossby wave packets. *Quart. J. Roy. Meteor. Soc.*, **144**, 553–566, https://doi.org/10.1002/qj.3228.

Fryirs, K., N. Zhang, T. J. Ralph, A. M. Arash, 2023: Natural flood management: Lessons and opportunities from the catastrophic 2021-2022 floods in eastern Australia. *Earth Surf. Proc. Landforms*, **48**, 1649-1664, https://doi.org/10.1002/esp.5647.

Gillett, Z., and Coauthors, 2023a: The State of Weather and Climate Extremes 2022. ARC Centre of Excellence for Climate Extremes, UNSW, Sydney, Australia. http://doi.org/10.26190/b0az-0920.

Gillett, Z. E., A. S. Taschetto, C. M. Holgate, and A. Santoso, 2023b: Linking ENSO to synoptic weather systems in eastern Australia. *Geophys. Res. Lett.*, **50**, e2023GL104814. https://doi.org/10.1029/2023GL104814.

Grab, S. W., and D. J. Nash, 2023: A new flood chronology for KwaZulu-Natal (1836-2022): the April 2022 Durban floods in historical context, *South African Geograph. J.*, https://doi.org/10.1080/03736245.2023.2193758.

Grazzini, F., G. Fragkoulidis, V. Pavan, and G. Antolini, 2020: The 1994 Piedmont flood: An archetype of extreme precipitation events in northern Italy. *Bull. Atmos. Sci. Technol.*, 1, 283–295, https://doi.org/10.1007/s42865-020-00018-1.

Accepted for publication in *Bulletin of the American Meteorological Society.* DOI 10.1175/BAMS-D-23-0141.1.

Grosfeld, N. H., S. McGregor, and. A. S. Tschetto, 2021: An automated climatology of cool-season cutoff lows over southeastern Australia and relationships with the remote climate drivers. *Mon. Wea. Rev.*, **149**, 4167-4181, https://doi.org/10.1175/MWR-D-21-0142.1.

Hart, R. E., and R. H. Grumm, 2001: Using normalized climatological anomalies to rank synoptic scale events objectively. *Mon. Wea. Rev.*, **129**, 2426– 2442, https://doi.org/10.1175/BAMS-D-19-0297.1.

Hart, N. C. G., C. J. C Reason, and N. Fauchereau, 2013: Cloud bands over southern Africa: Seasonality, contribution to rainfall variability and modulation by the MJO. Climate Dyn., 41, 1199–1212, https://doi.org/10.1007/s00382-012-1589-4.

Hart, N. C. G., R. Washington, and C. J. C Reason, 2018: On the likelihood of tropical-extratropical cloud bands in the South Indian Convergence Zone during ENSO events, J. Climate, 31, 2797-2817, https://doi.org/10.1175/JCLI-D-17-0221.1.

Hauser, S., C. M. Grams, M. J. Reeder, S. McGregor, A. H. Fink, and J. F. Quinting, 2020: A weather system perspective on winter–spring rainfall variability in southeastern Australia during El Niño. *Quart. J. Roy. Meteor. Soc.*, **146**, 2614–2633, https://doi.org/10.1002/qj.3808.

Henderson, S., E. Maloney, and E. Barnes, 2016: The influence of the Madden–Julian Oscillation on Northern Hemisphere winter blocking. *J. Climate*, **29**, 4597–4616, doi:10.1175/JCLI-D-15-0502.1.

Henderson, G. R., B. S. Barrett, A. Lois, and H. Elsaawy, 2018: Time-lagged response of the Antarctic and high-latitude atmosphere to tropical MJO convection. *Mon. Wea. Rev.*, **146**, 1219-1231, https://doi.org/10.1175/MWR-D-17-0224.1.

Henderson C. R., M. J. Reeder, T. J. Parker, J. F. Quinting, and C. Jakon (2024), Summer heatwaves in southeastern Australia. *Quart. J. Roy. Meteor. Soc.*, **150**, 4285–4305, https://doi.org/10.1002/qj.4816.

Hepworth, E., G. Messori, G., and M. Vichi, 2022: Association between extreme atmospheric anomalies over Antarctic sea ice, Southern Ocean polar cyclones and atmospheric rivers. *J. Geophys. Res. Atmospheres*, **127**, e2021JD036121. https://doi.org/10.1029/2021JD036121.

Hersbach, H., and Coauthors, 2020: The ERA5 global reanalysis. *Quart. J. Roy. Meteor. Soc.*, **146**, 1999–2049, https://doi.org/10.1002/qj.3803.

Accepted for publication in *Bulletin of the American Meteorological Society.* DOI 10.1175/BAMS-D-23-0141.1.

Hoell, A., C. Funk, T. Magadzire, J. Zinke, and G. Husak, 2015: El Niño-Southern Oscillation diversity and southern Africa teleconnections during austral summer. *Climate Dyn.*, **45**, 1583–1599, https://doi.org/10.1007/s00382-014-2414-z.

Holgate, C., J. P. Evans, A. S. Taschetto, A. S., Gupta, and A. Santoso, 2022: The impact of interacting climate modes on east Australian precipitation moisture sources. *J. Climate*, **35**, 3147–3159, https://doi.org/10.1175/JCLI-D-21-0750.1.

Holgate, C. M., A. S. Pepler, I. Rudeva, N. J. Abram, 2023: Anthropogenic warming reduces the likelihood of drought-breaking extreme rainfall events in southeast Australia. *Wea. Climate Extremes*, **42**, 100607, https://doi.org./10.1016/j.wace.2023.100607.

Hsu, P.-C., Z. Fu, H. Murakami, J.-Y. Lee, C. Yoo, N. Johnson, C.-H. Chang, and Y. Liu (2021), East Antarctic cooling induced by decadal changes in Madden-Julian oscillation during austral summer, Science Adv., 7, https://doi.org/10.1126/sciadv.abf9903.

Huang, B., P., and Coauthors, 2017: Extended reconstructed Sea surface temperature, Version 5 (ERSSTv5): Upgrades, validations, and intercomparisons. *J. Climate*, **30**, 8179-8205, https://doi.org/10.1175/JCLID-16-0836.1.

Huang, A. T., Z. E. Gillett, and A. S. Taschetto, 2024: Australian rainfall increases during multi-year La Niña. *Geophys. Res. Lett.*, **51**, e2023GL106939, https://doi.org/10.1029/2023GL106939.

Huffman, G. J., Bolvin, T. D., Braithwaite, D., Hsu, K.-L. Joyce, R. J., Kidd, C., Nelkin, E. J., Sorooshian, S., Stocker, E. F., Tan, J., Wolff, D. B., & Zie, P. Integrated multi-satellite retrievals for the Global Precipitation Measurement (GPM) Mission (IMERG). Adv. Glob. Change Res., 67, 343-353, https://doi.org/10.1007/978-3-030-24568-9_19 (2020).

Irving, D., and I. Simmonds, 2016: A new method for identifying the Pacific–South American pattern and its influence on regional climate variability. *J. Climate*, **29**, 6109–6125, https://doi.org/10.1175/JCLI-D-15-0843.1.

Ivanciu, I., T. Ndarana, K. Matthes, and S. Wahl, 2022: On the ridging of the South Atlantic Anticyclone over South Africa: The impact of Rossby wave breaking and of climate change. *Geophys. Res. Lett.*, **49**, e2022GL099607, https://doi.org/10.1029/2022GL099607.

Accepted for publication in *Bulletin of the American Meteorological Society.* DOI 10.1175/BAMS-D-23-0141.1.

Jin C., M. J. Reeder, A. J. E. Gallant, T. Parker, M. Sprenger (2024), Changes in weather systems during anomalously wet and dry years in southeastern Australia. *J. Climate*, **37**, 1131-1153, https://doi.org/10.1175/JCLI-D-23-0305.1.

King, A. D., L. V. Alexander, and M. G. Donat, 2013: Asymmetry in the response of eastern Australia extreme rainfall to low-frequency Pacific variability. *Geophys. Res. Lett.*, **40**, 2271–2277, https://doi.org/10.1002/grl.50427.

King, A. D., N. P. Klingaman, L. V. Alexander, M. G. Donat, N. C. Jourdain, and P. Maher, 2014: Extreme rainfall variability in Australia: Patterns, drivers, and predictability. *J. Climate*, **27**, 6035–6050, https://doi.org/10.1175/JCLI-D-13-00715.1.

King, A. D., K. J. Reid, and K. R. Saunders, 2023: Communicating the link between climate change and extreme rain events. *Nat. Geosc.*, **16**, 552–554, https://doi.org/10.1038/s41561-023-01223-1.

Li, X., and Coauthors, 2021: Tropical teleconnection impacts on Antarctic climate changes. *Nat. Rev. Earth Environ.*, **2**, 680–698, https://doi.org/10.1038/s43017-021-00204-5.

Madden, R. A., and P. R. Julian, 1972: Description of global-scale circulation cells in the tropics with a 40-50 day period. *J. Atmos. Sci.*, **29**, 1109–1123, https://doi.org/10.1175/1520-0469(1971)028<0702:DOADOI>2.0.CO;2.

Marengo, J. A., and Coauthors, 2023: Flash floods and landslides in the city of Recife, Northeast Brazil after heavy rain on May 25–28, 2022: Causes, impacts, and disaster preparedness. Weather and Climate Extremes, 39, 100545, https://doi.org/10.1016/j.wace.2022.100545.

Martius, O., C. Schwierz, and H. C. Davies, 2008: Far-upstream precursors of heavy precipitation events on the Alpine south-side. *Quart. J. Roy. Meteor. Soc.*, **134**, 417–428, https://doi.org/10.1002/qj.229.

Mashao, F.M., M. C. Mothapo, R. B. Munyai, J. M. Letsoalo, I. L. Mbokodo, T. P. Muofhe, W. Matsane, and H. Chikoore, 2023: Extreme Rainfall and Flood Risk Prediction over the East Coast of South Africa. *Water*, **15**, 50. https://doi.org/10.3390/w15010050.

Massey, F. J., 1951: The Kolmogorov-Smirnov Test for Goodness of Fit. *J. Amer. Statist. Ass.*, **46**, 68–78. https://doi.org/10.2307/2280095.

Accepted for publication in *Bulletin of the American Meteorological Society.* DOI 10.1175/BAMS-D-23-0141.1.

McKay, R. C., and Coauthors, 2023: Can southern Australian rainfall decline be explained? A review of possible drivers. *Wiley Interdiscip. Rev.: Climate Change*, **14**, e820, https://doi.org/10.1002/wcc.820.

Messori, G., C. Woods, and R. Caballero, 2018: On the drivers of wintertime temperature extremes in the high Arctic. *J. Climate*, **31**, 1597–1618, https://doi.org/10.1175/JCLI-D-17-0386.1.

Muñoz, C., and D. M. Schultz, 2021: Cutoff lows, moisture plumes, and their influence on extreme-precipitation days in central Chile. *J. Applied Meteor. Climatol.*, **60**, 437-454, https://doi.org/10.1175/JAMC-D-20-0135.1.

Ndarana, T., and D. W. Waugh (2010), The link between cut-off lows and Rossby wave breaking in the Southern Hemisphere. *Quart. J. Roy. Meteor. Soc.*, **136**, 869-885, https://doi.org/10.1002/qj.627.

Ndarana, T., M. J. Bobape, D. Waugh, L. Dyson, (2018), The influence of the lower stratosphere on ridging Atlantic Ocean anticyclones over South Africa. *J. Climate,*31, 6175-6187, https://doi.org/10.1175/JCLI-D-17-0832.1.

Ndarana, T., S. Mpati, M.-J. Bobape, F. Engelbrecht, H. Chikoore (2020), The flow and moisture fluxes associated with ridging South Atlantic anticyclones during the subtropical southern African summer. *Int. J. Clim.*, 41, https://doi.org/10.1002/joc.6745.

Ndarana, T., L. E. Lekoloane, T. S. Rammopo, C. J. C. Reason, M. M. Bopape, H. Chikoore, F. E. Engelbrecht, 2023: Downstream development during ridging South Atlantic Ocean anticyclones. *Climate Dyn.*, **61**, 2865-2883, https://doi.org/10.1007/s00382-023-06717-7.

Liu, C., and E. A. Barnes, 2015: Extreme moisture transport into the Arctic linked to Rossby wave breaking. *J. Geophys. Res.*, **120**, 3774–3788, https://doi.org/10.1002/2014JD022796.

Orr, A., and Coauthors, 2023: Characteristics of surface “melt potential” over Antarctic ice shelves based on regional atmospheric model simulations of summer air temperature extremes from 1979/80 to 2018/19. *J. Climate*, **36**, 3357–3383, https://doi.org/10.1175/JCLI-D-22-0386.1.

Otto F. E. L., and Coauthors, 2022: Climate change increased rainfall associated with tropical cyclones hitting highly vulnerable communities in Madagascar, Mozambique & Malawi. Word Weather Attribution Service. https://www.worldweatherattribution.org/climate-

Accepted for publication in *Bulletin of the American Meteorological Society.* DOI 10.1175/BAMS-D-23-0141.1.

change-increased-rainfall-associated-with-tropical-cyclones-hitting-highly-vulnerable-communities-in-madagascar-mozambique-malawi/.

Parker T. J., G. J. Berry, and M. J. Reeder (2014), The structure and evolution of heat waves in southeastern Australia. *J. Climate*, **27**, 5768–5785, https://doi.org/10.1175/JCLI-D-13-00740.1.

Pérez-Fernández, I., M. Barreiro, N. Ehstand, E. Hernández-García, C. López (2024), Wave breaking events and their links to Rossby wave packets and atmospheric blockings during southern Hemisphere summer. *J. Geophys. Res. Atmos.*, **129,** *e2022JD038380.* https://doi.org/10.1029/2022JD038380.

Perkins-Kirkpatrick, S., and S. Lewis, S. 2020: Increasing trends in regional heatwaves. *Nature Commun.*, **11**, 1–8. https://doi.org/10.1038/s41467-020-16970-7.

Pinheiro H. R., K. I. Hodgers, and M. A. Gan (2024), Deepening mechanisms of cut-off lows in the Southern Hemisphere and the role of jet streams: insights from eddy kinetic energy analysis. *Wea. Climate Dyn.*, **5**, 881-894, https://doi.org/10.5194/wcd-5-881-2024.

Pinto I, and Coauthors, 2022: Climate change exacerbated rainfall causing devastating flooding in Eastern South Africa. World Weather Attribution. https://www.worldweatherattribution.org/wp-content/uploads/WWA-KZN-floods-scientific-report.pdf.

Portmann, R., M. Sprenger, and H. Wernli (2021), The three-dimensional life cycles of potential vorticity cutoffs: a global and selected regional climatologies in ERA-Interim (1979-2018). *Wea. Clim. Dyn.*, 2, 507-534, https://doi.org/10.5194/wcd-2-507-2021.

Preece, J. R., L. J. Wachowicz, T. L. Mote, M. Tedesco, and X. Fettweis, 2022: Summer Greenland blocking diversity and its impact on the surface mass balance of the Greenland Ice Sheet. *J. Geophys. Res. Atmos.*, **127**, e2021JD035489, https://doi.org/10.1029/2021JD035489.

Reid, K. J., M. A. Barnes, Z. E. Gillett, T. Parker, D. G. Udy, H. Ayat, G. Boschat, A. Bowden, N. H. Grosfeld, A. D. King, D. Richardson, Y. Shao, L. Teckentrup, B. Trewin, P. Hope, L. Zhou, A. R. Borowiak, C. M. Holgate, and R. N. Isphording (2025), A multiscale evaluation of the wet 2022 in eastern Australia, *J. Climate*, **38**, 909-929, https://doi.org/10.1175/JCLI-D-24-0224.1.

Accepted for publication in *Bulletin of the American Meteorological Society.* DOI 10.1175/BAMS-D-23-0141.1.

Reyers, M., C. Böhm, L. Knarr, Y. Shao, and S. Crewell, 2020: Synoptic-to-regional scale analysis of rainfall in the Atacama Desert (18°S–26°S) using a long-term simulation with WRF. *Mon. Wea. Rev.*, **149**, 91–112, https://doi.org/10.1175/MWR-D-20-0038.1.

Risbey, J. S., M. J. Pook, P. C. McIntosh, M. C. Wheeler, and H. H. Hendon, 2009: On the remote drivers of rainfall variability in Australia. *Mon. Wea. Rev.*, **137**, 3233–3253, https://doi.org/10.1175/2009MWR2861.1.

Rondanelli, R., B. Hatchett, J. Rutllant, D. Bozkurt, and R. Garreaud, 2019: Strongest MJO on record triggers extreme Atacama rainfall and warmth in Antarctica. *Geophys. Res. Lett.*, **46**, 3482–3491. https://doi.org/10.1029/2018GL081475.

Röthlisberger, M., L. Frossard, L. F. Bosart, D. Keyser, and O. Martius, 2019: Recurrent synoptic-scale Rossby wave patterns and their effect on the persistence of cold and hot spells. *J. Climate*, **32**, 3207–3226, https://doi.org/10.1175/JCLI-D-18-0664.1.

Röthlisberger, M., and L. Papritz, 2023: Quantifying the physical processes leading to atmospheric hot extremes at a global scale. *Nat. Geosci.*, **16**, 210–216, https://doi.org/10.1038/s41561-023-01126-1.

Russo, S., J. Sillmann, and E. Fischer, 2015: Top ten European heatwaves since 1950 and their occurrence in the coming decades. *Environ. Res. Lett.*, **10**, 124003, https://doi.org/10.1088/1748-9326/10/12/124003.

Russo, E., and D. I. V. Domeisen, 2023: Increasing intensity of extreme heatwaves: The crucial role of metrics. *Geophys. Res. Lett.*, **50**, e2023GL103540. https://doi.org/10.1029/2023GL103540

Schlemmer, L., O. Martius, M. Sprenger, C. Schwierz, and A. Twitchett, 2010: Disentangling the forcing mechanisms of a heavy precipitation event along the alpine south side using potential vorticity inversion. *Mon. Wea. Rev.*, **138**, 2336–2353, https://doi.org/10.1175/2009MWR3202.1.

Schmid, T., V. Radić, A. Tedstone, J. M. Lea, S. Brough, M. and Hermann (2023), Atmospheric drivers of melt-related ice speed-up events on the Russell Glacier in southwest Greenland. *Cryosph.*, **17**, 3933–3954, https://doi.org/10.5194/tc-17-3933-2023.

Schwendike, J., G. J. Berry, K. Fodor, and M. J. Reeder, 2021: On the relationship between the Madden-Julian Oscillation and the Hadley and Walker circulations. *J. Geophys. Res. Atmos.*, **126**. https://doi.org/10.1029/2019JD032117.

Accepted for publication in *Bulletin of the American Meteorological Society.* DOI 10.1175/BAMS-D-23-0141.1.

Siegert, M. J., M. J. Bentley, A. Atkinson, T. J. Bracegirdle, P. Convey, B. Davies, R. Downie, A. E. Hogg, C. Holmes, K. A. Hughes, M. P. Meredith, N. Ross, J. Rumble, and J. Wilkinson, 2023: Antarctic extreme events. *Front. Environ. Sci.*, **11**:1229283. https://doi.org/10.3389/fenvs.2023.1229283.

Simon, S., J. Turner, M. Thamban, J. D. Wille, and P. Deb, 2024: Spatiotemporal variability of extreme precipitation events and associated atmospheric processes over Dronning Maud Land, East Antarctica. *J. Geophys. Res. Atmospheres*, **129**, e2023JD038993. https://doi.org/10.1029/2023JD038993.

Singleton, A. T., and C. J. C. Reason, 2007: Variability in the characteristics of cut-off low pressure systems over subtropical southern Africa. *Int. J. Climatol.*, **27**, 295–310, https://doi.org/10.1002/joc.1399.

Skerlak, B., M. Sprenger, S. Pfahl, E. Tyrlis, and H. Wernli, 2015: Tropopause folds in ERA-Interim: Global climatology and relation to extreme weather events, *J. Geophys. Res. Atmos.*, **120**, 4860-4877, https://doi.org/10.1002/2014JD022787.

Sprenger, M., O. Martius, and J. Arnold, 2013: Cold surge episodes over southeastern Brazil - a potential vorticity perspective, *Int. J. Climatol.*, **33**, 2758-2767, https://doi.org/10.1002/joc.3618.

Sprenger, M., and Coauthors, 2017: Global climatologies of Eulerian and Lagrangian flow features based on ERA-Interim. *Bull. Amer. Meteor. Soc.*, **98**, 1739–1748, https://doi.org/10.1175/BAMS-D-15-00299.1.

Sun, X., B. Renard, M. Thyer, S. Westra, and M. Lang, 2015: A global analysis of the asymmetric effect of ENSO on extreme precipitation. *J. Hydrol.*, **530**, 51–65, https://doi.org/10.1016/j.jhydrol.2015.09.016.

Tamarin-Brodsky, T. and N. Harnik (2024), The relation between Rossby wave-breaking events and low-level weather systems. *Wea. Clim. Dyn.*, **5**, 87–108, https://doi.org/10.5194/wcd-5-87-2024.

Tedesco, M., and Coauthors, 2016: Arctic cut-off high drives the poleward shift of a new Greenland melting record. *Nat. Commun.*, **7**, 11723, https://doi.org/10.1038/ncomms11723.

Accepted for publication in *Bulletin of the American Meteorological Society*. DOI 10.1175/BAMS-D-23-0141.1.

Tencaliec, P., A. C. Favre, P. Naveau, C. Prieur, and G. Nicolet, 2019: Flexible semiparametric generalized Pareto modeling of the entire range of rainfall amount. *Environmetrics*, **31**, e2582, https://doi.org/10.1002/env.2582.

Thoithi, W., R. Blamey, and C. Reason, 2023: April 2022 Floods over East Coast South Africa: Interactions between a Mesoscale Convective System and a Coastal Meso-Low. *Atmosphere*, **14**, 78. https://doi.org/10.3390/atmos14010078.

Turner, J., H. Lu, J. King, G. J. Marshall, T. Phillips, D. Bannister, and S. Colwell, 2021: Extreme temperatures in the Antarctic. *J. Climate*, **34**, 2653–2668, https://doi.org/10.1175/JCLI-D-20-0538.1.

Turner, J., H. Lu, J. King, S. Carpentier, M. Lazzara, T. Phillips, and J. Wille, 2022: An extreme high temperature event in coastal East Antarctica associated with an atmospheric river and record summer downslope winds. *Geophys. Res. Lett.*, **49**, e2021GL097108, https://doi.org/10.1029/2021GL097108.

Ullah, A., B. Pohl, J. Pergaud, B. Dieppois, and M. Rouault, 2023: Intraseasonal descriptors and extremes in South African rainfall. Part II: Summer teleconnections across multiple timescales. *Int. J. Climatol.*, **43**(8), 3799–3827, https://doi.org/10.1002/joc.8059.

Wang, S., and Coauthors, 2023: New record of explosive warmings in East Antarctica. *Sci. Bull.*, **68**, 129–132, https://doi.org/10.1016/j.scib.2022.12.013.

Ward, P. J., S. Eisner, M. Flörke, M. D. Dettinger, M. Kummu, 2014: Annual flood sensitivities to El Niño-Southern Oscillation at the global scale. *Hydrol. Earth Syst. Sci.*, **18**, 47–66, https://doi.org/10.5194/hess-18-47-2014.

Warren, R. A., C. Jakob, S. M. Hitchcock, B. A. and White, 2021: Heavy versus extreme rainfall events in Southeast Australia. *Quart. J. Roy. Meteor. Soc.*, **147**, 3201–3226 https://doi.org/10.1002/qj.4124.

Welker, C., O. Martius, P. Froidevaux, C. H. Reijmer, and H. Fischer (2014), A climatological analysis of high-precipitation events in Dronning Maud Land, Antarctica, and associated large-scale atmospheric conditions. *J. Geophys. Res. Atmos.*, **119**, 932–954, https://doi.org/10.1002/2014JD022259.

Wernli, H., and M. Sprenger, 2007: Identification and ERA-15 climatology of potential vorticity streamers and cutoffs near the extratropical tropopause, *J. Atmos. Sci.*, **64**, 1569–1586, https://doi.org/10.1175/JAS3912.1.

Accepted for publication in *Bulletin of the American Meteorological Society.* DOI 10.1175/BAMS-D-23-0141.1.

Wernli, H., and L. Papritz, 2018: Role of polar anticyclones and midlatitude cyclones for Arctic summertime sea-ice melting. *Nat. Geosci.*, **11**, 108–114, https://doi.org/10.1038/s41561-017-0041-0.

Wheeler, M. C., and H. H. Hendon, 2004: An all-season real-time multivariate MJO index: Development of an index for monitoring and prediction. *Mon. Wea. Rev.*, **132**, 1917–1932.

Wheeler, M. C., H. H. Hendon, S. Cleland, H. Meinke, and A. Donald, 2009: Impacts of the MJO on Australian rainfall and circulation. *J. Climate*, **22**, 1482–1497, https://doi.org/10.1175/2008JCLI2595.1.

Wicker, W., N. Harnik, M. Pyrina, D. I. V. and Domeisen, 2024: Heatwave location changes in relation to Rossby wave phase speed. *Geophys. Res. Lett.*, **51**, e2024GL108159. https://doi.org/10.1029/2024GL108159.

Wille, J. D., V. Favier, A. Dufour, I. V. Gorodetskaya, J. Turner, C. Agosta, and F. Codron, 2019: West Antarctic surface melt triggered by atmospheric rivers. *Nat. Geosci.*, **12**, 911–916, https://doi.org/10.1038/s41561-019-0460-1.

Wille, J. D., and Coauthors, 2022: Intense atmospheric rivers can weaken ice shelf stability at the Antarctic Peninsula. *Commun. Earth Environ.*, **3**, 90, https://doi.org/10.1038/s43247-022-00422-9.

Wille, J. D., and Coauthors, 2024a: The extraordinary March 2022 East Antarctica "heat" wave. Part I: Observations and meteorological drivers. *J. Climate*, **37**, 757–778, https://doi.org/10.1175/JCLI-D-23-0176.s1.

Wille, J. D., and Coauthors, 2024: The extraordinary March 2022 East Antarctica "heat" wave. Part II: Impacts on the Antarctic ice sheet. *J. Climate*, **37**, 779–799, https://doi.org/10.1175/JCLI-D-23-0176.1.

Woods, C., R. Caballero, and G. Svensson, 2013: Large-scale circulation associated with moisture intrusions into the Arctic during winter. *Geophys. Res. Lett.*, **40**, 4717–4721, https://doi.org/10.1002/grl.50912.

Woollings, T., and Coauthors, 2023: The role of Rossby waves in polar weather and climate, *Wea. Climate Dyn.*, **4**, 61–80, https://doi.org/10.5194/wcd-4-61-2023.

Xin, M., K. R. Clem, J. Turner, S. E. Stammerjohn, J. Zhu, W. Cai, and X. Li, 2023: West-warming East-cooling trend over Antarctica reversed since early 21st century driven by

Accepted for publication in *Bulletin of the American Meteorological Society.* DOI 10.1175/BAMS-D-23-0141.1.

large-scale circulation variation. *Environ. Res. Lett.*, **18**, 064034, https://doi.org/10.1088/1748-9326/acd8d4.

Zhang, C., 2013: Madden–Julian oscillation: Bridging weather and climate. *Bull. Amer. Meteor. Soc.*, **94**, 1849–1870, https://doi.org/10.1175/BAMS-D-12-00026.1.

Zhang, G., and Coauthors, 2021: Seasonal predictability of baroclinic wave activity, *npj Clim. Atm. Sci.*, **5**, https://doi.org/10.1038/s41612-021-00209-3.

Accepted for publication in *Bulletin of the American Meteorological Society.* DOI 10.1175/BAMS-D-23-0141.1.